Title
Identification of arbitrarily shaped scatterers embedded in elastic heterogeneous media using dynamic XFEM

Author
Jung, Jaedal

Publication Date
2014

Peer reviewed|Thesis/dissertation

University of California
Los Angeles

Identification of arbitrarily shaped scatterers embedded in elastic heterogenous media using dynamic XFEM

A dissertation submitted in partial satisfaction
of the requirements for the degree
Doctor of Philosophy in Mechanical and Aerospace Engineering

by

Jaedal Jung

2014

Abstract of the Dissertation

Identification of arbitrarily shaped scatterers embedded in elastic heterogenous media using dynamic XFEM

by

Jaedal Jung

Doctor of Philosophy in Mechanical and Aerospace Engineering

University of California, Los Angeles, 2014

Professor Ertugrul Taciroglu, Co-chair

Professor Christopher S. Lynch, Co-chair

Numerical approaches for localization and shape quantification of multiple arbitrarily-shaped scatterers (cracks, voids, and inclusions) embedded in heterogenous linear elastic media are described. A dynamic extended finite element method (XFEM) equipped with scatterer-boundary parameterizations using cubic splines is used to solve the forward (wave propagation) problem. The said combination enables the modeling of scatterer boundaries with complex geometries over a stationary background mesh. The inverse problem is cast as an optimization problem whereby an appropriate measure of the discrepancies between wave responses obtained from forward simulations and those that are measured from the actual specimen is minimized. A gradient-based minimization that is steered with a divide-alternate-and-conquer strategy serves as the inverse problem solver. The divide-and-conquer approach enables isolating the global minimizer among potentially multiple solutions, and the alternate-and-conquer approach enhances the former strategy to tackle multiple scatterers. The approaches developed herein are verified using using numerical experiments (i.e., synthetic data sets) involving different types of scatterers. Effects of measurement noise are also investigated.

The dissertation of Jaedal Jung is approved.

Stanley B. Dong

Nasr M. Ghoniem

William S. Klug

Christopher S. Lynch, Committee Co-chair

Ertugrul Taciroglu, Committee Co-chair

University of California, Los Angeles

2014

Dedicated to my family

Table of Contents

List of Figures

List of Tables

Acknowledgments

First and foremost, I would like to express my sincerest gratitude to my advisor, Prof. Ertugrul Taciroglu in the Department of Civil and Environmental Engineering, for his unstinting support, his faith in my abilities, and his careful consideration in my winding journey towards the doctoral degree. His insightful advice kept me on the right path and it would not have been possible to complete my doctoral dissertation without his warm encouragement and unconditional support.

I also owe a debt of gratitude to my thesis committee: Prof. Christopher S. Lynch, a co-advisor in the Department of Mechanical and Aerospace Engineering, gave me meticulous advice and great help in the preparation of my career after the Ph.D. degree; Prof. Stanely B. Dong not only helped me learn the semi-analytical finite element method, but also endowed me with critical knowledge on mechanics of composite materials and wave propagation analysis; Prof. Nasr Ghoniem and Prof. William S. Klug gave me constructive comments and questions.

I would like to thank my UCLA Korean Graduate Student Association (KGSA) basketball team, Jesse Ko, Jin Park, Dongyeop Kwak, Jungin Choi, Andre Kim, Sangjo Jeong, Hanjun John Kim, Donghyuk Kim, Mintaek Yoo and Hyungseok Kim, for all the fun and unforgettable memories we had together. I also would like to express my gratitude to my lab-mates, Seyedali Nojoumi, Elnaz Esmaeilzadeh Seylabi, Richard J. H. Gash, and Barbaros Cetiner, for their great respect and regard. In particular, I would like to express the deepest appreciation to my friends, Dr. Chanseok Jeong and Dr. Eon Lee, for having constructive discussions, which lead to the preparation of new journal articles.

Last but not least, I would like to thank my family, my parents, Woosub Jung and Soonhee Jang, and my younger brother, Jaeyeob Jung, for their steadfast support and caring, and endless love.

Vita

2004	B.E. (Mechanical Engineering), Seoul National University of Science & Technology.
2004–2006	Research Assistant, Mechanical Engineering Department, Yonsei University.
2006	M.S. (Mechanical Engineering), Yonsei University.
2009	Teaching Assistant, Mechanical & Aerospace Engineering Department, UCLA. - MAE 101. Statics and Strength of Materials.
2011–present	Teaching Assistant, Civil & Environmental Engineering Department, UCLA. - CEE 103, Applied Numerical Computing and Modeling. - CEE 235A, Advanced Structural Analysis. - CEE 130, Elementary Structural Mechanics. - CEE 135A, Elementary Structural Analysis. - CEE 108, Introduction to Mechanics of Deformable Solids. - CEE 135L, Structural Design and Testing Lab.

Publications

J. Jung, S. Cho, and C. Lee, "Behavior of a heavy particle in the shear flow near a flat wall," *Korean Society of Mechanical Engineering B*, 30, 806, 2006.

J. Jung, K. Yeo, and C. Lee, "Behavior of heavy particles in isotropic turbulence," *Physical Review E*, 77, 016307, 2008.

C. Lee, Y. Park, and **J. Jung**, "Source of acceleration intermittency in isotropic turbulence," *Journal of Mechanical Science and Technology*, 26, 3843-3847, 2012.

J. Jung, C. Jeong, and E. Taciroglu, "Identification of a scatterer embedded in elastic heterogeneous media using dynamic XFEM," *Computer Methods in Applied Mechanics and Engineering*, 259, 50-63, 2013.

J. Jung, and E. Taciroglu, "Modeling and identification of an arbitrarily shaped scatterer using dynamic XFEM with cubic splines," *Computer Methods in Applied Mechanics and Engineering*, 278, 101-118, 2014.

J. Jung, and E. Taciroglu, "A divide-alternate-and-conquer strategy for shape identification of multiple arbitrarily shaped scatterers using dynamic XFEM," (under preparation).

CHAPTER 1

Introduction

1.1 An overview of vibration-based damage identification techniques

Identification of damage in structures and structural components is a vast subject comprising many threads of inquiry. A large branch is devoted to vibration-based damage identification techniques using acceleration data in the low-frequency range, typically less than 100 Hz. These efforts include identifying structures' or structural components' modal characteristics through measurements made with acceleration/velocity transducers—placed strategically within the structure—during ambient vibration surveys or forced vibration testing with linear of eccentric shakers (see, for example, Yu et al., 2007). These data are then analyzed to identify and quantify damage within the specimen. This area is generally referred to as "*condition monitoring*" when applied to mechanical systems (e.g., an engine block) or "*structural health-monitoring*" when applied to civil structures (e.g., a multi-story building). Developments in this area have been well summarized in various surveys such as that by Doebling et al. (1998).

The present research focuses in a different, yet in many ways, closely related application area, which is typically collectively referred to as nondestructive testing (NDT). Again, the literature on NDT is vast—essentially going back to the works of Sokolov (1935), and Firestone (1950)[1]. Today, NDT data collection and

[1]See, the book by Graff (1982) Graff (1982) for a detailed survey of the history of ultrasonic testing and evaluation.

interpretation techniques are diverse, and application areas range from mechanical engineering to medicine (Shull, 2002).

The scope of present research is limited to the inspection of defects (e.g., akareflectors, scatterers, discontinuities) using waves that are excited in the acoustic/ultrasonic range of frequencies (i.e., 500 kHz to 25 MHz). In a broad sense, damage-identification methods can be classified into four levels. Quoting Doebling et al. (1998), these levels are:

- "Level 1: Determination that damage is present in the structure,
- Level 2: L1 plus determination of the location of the damage,
- Level 3: L2 plus quantification of the severity of the damage,
- Level 4: L3 plus prediction of the remaining service life of the structure."

Even to the present day, vibration-based methods primarily provide only Level 1 and Level 2 damage identification. When a structural model is employed to interpret the measurements, it is sometimes possible to attain a Level 3 identification. Level 4 is essentially the utilization of the quantified damage information, and this area typically combines Level 3 data into predictive formulas derived from fracture/damage/fatigue mechanics, durability, etc.

Level 1 damage identification consists primarily of calculating frequency shifts from a known type of damage. This approach is showcased in the study by Juneja et al., 1997 who developed a "contrast maximization" technique in which they match the response of the damaged structure to a database of structural responses. The inverse problem, which is typically Level 2 or Level 3 damage identification, consists of calculating the damage parameters—i.e., crack length and location—from data. Lifshitz and Rotem's (1969) work is among the first in which such solutions were pursued. A similar study—wherein a model of the

structure was utilized in the damage detection problem—was carried out by Lynn and Kumbasar (1967) who analyzed free vibration behavior of cracked rectangular plates using a Green's function. In later studies, the vibration characteristics of rectangular plates with cracks was investigated using Fourier series by Hirano and Okazaki (1980); and Bayissa and Haritos (2007) proposed a new damage identification technique based on the statistical moments of the energy density function of the vibration responses in the time-scale domain. Some of the recent work focused on the use of wavelet analysis for damage identification (see, for example, Rizzo and di Scalea, 2005; Rucka and Wilde, 2006; Bayissa et al., 2008; Bagheri et al., 2009).

In conventional ultrasound methods (Krautkrämer and Krautkrämer, 1990), the excitation is typically provided in the form of a band-limited pulse with center frequencies ranging from 100 kHz - 15 MHz using an ultrasonic transducer. The basic ultrasonic approaches to the damage identification problem are the, so-called, "pulse-echo" or "pitch-catch" techniques. In the former, the transducer (actuator) also acts as the receiver (sensor); while in the latter, transducer and the receiver are not collocated. In either case, the generated waves are reflected by the scatterer; and the arrival times and amplitudes of the received waves are used for a Level 2 diagnostic. The advantages of these approaches include their ability to detect even very small flaws that are located deeply in the tested specimen. The basic disadvantage is the need to be close to the defect and the limited level of information that may be gleaned from the data.

1.2 Motivation and background

Identification and quantification of hidden scatterers (e.g., damage or defects such as cracks, voids, and inclusions) in an incipient stage before a fracture occurs in structures is an integral part in predictive maintenance as well as structural health

monitoring (SHM) (Doebling et al., 1998; Hellier, 2003). Ultrasonic inspection—one of the well-established nondestructive evaluation (NDE) methods for assessing the current state of a structural system—has been widely applied in various areas such as SHM (Hellier, 2003), medical imaging (Fatemi and Greenleaf, 1999; Urban et al., 2011) and geophysical prospecting (Jia et al., 2002; Wijk, 2003). In a typical ultrasonic inspection, a single actuator and multiple sensors are positioned along the boundary of the host medium. Mechanical waves produced by the actuators travel through the medium and are reflected/refracted when encountering internal scatterers. From the wave signals returning back to each sensor, their locations and sizes are identified. Such an approach utilizing ultrasonic waves, however, has difficulties in the precise reconstruction of multiple scatterers within a heterogeneous medium (Rose, 1989). This is primarily due to the interference/superposition of multiply scattered waves from the scatterers (Wijk, 2003) and the wave reflections from the internal interfaces between two media with different types of property (Zou et al., 2000). For accurate estimation of buried scatterers, more sophisticated and systematic identification approaches based on the finite element method (FEM) and the boundary element method (BEM) have recently been proposed for different application areas (see, for example, Bonnet and Guzina, 2009; Brigham et al., 2007; Kallivokas et al., 2013; Yuan and Guzina, 2012).

In general, parameter identification (here, inverse-scattering) problems can be cast as minimization problems, wherein an objective (aka *cost* or *error*) functional that quantifies the discrepancy between predictions of measurements form a forward simulation run with a parametric model, and the measurements—e.g., displacements obtained via ultrasonic testing—themselves (Liu and Han, 2003). The said identification process (here, seeking first the location, and subsequently, the optimal shape parameters of the scatterers) requires two main ingredients: (*i*) an accurate forward modeling method; and (*ii*) a robust optimization algo-

rithm. The forward modeling predictions of measurements can be obtained for a given set of iteratively estimated scatterer (aka *updating*) parameters. In the inversion process, these parameters—describing the shape, size, and location of each scatterer—are updated using a proper optimization method that steers them towards the minimizer(s) of the objective functional.

A classical challenge in shape optimization and identification methods is the need to employ an adequately general method for forward simulations—so that, for example, arbitrary loading and boundary conditions, material heterogeneities, and different sensor-actutor deployment schemes can be handled. As such, the classical finite element method, at first, appears to be suitable choice for generating forward simulations. However, iterative refinement of the location and the shape of the scatterer(s) pose a significant challenge, in that the classical FEM would require re-meshing of the entire domain for every iteration. This issue is not only a challenge because of potentially intractable computational costs, but also because of lack of robust and adequately general automatic re-meshing methods for arbitrary domain geometries and topologies, as well as element types (Edelsbrunner, 2001). In this thesis, this critical issue will be circumvented through the adoption of the so-called eXtended Finite Element Method (XFEM), which obviates re-meshing during the minimization procedure.

Since its inception by Belytschko and Black in 1999, XFEM has been continuously improved, and utilized in a variety of applications, including the modeling of crack propagation (Richardson et al., 2011), material interfaces and dislocations (Belytschko and Gracie, 2007), multi-phase and free-surface flows (Sauerland and Fries, 2013), bone fracture (Feericka et al., 2013), and biofilms (Smith et al., 2007) to name a few. As stated above, XFEM is very well-suited for shape identification and optimization problems because (i) re-meshing procedures are not required to render the background mesh to conform perfectly to the arbitrarily evolving boundary of a scatterer during an iterative identification procedure (Benowitz

and Waisman, 2013; Jung and Taciroglu, 2014); and (*ii*) the host medium can be arbitrarily heterogenous and anisotropic (Sukumar et al., 2001).

A key issue a in any generic inverse problem is to filter out multiple erroneous solutions (local minima), which inherently originate due to temporal and spatial sparseness of the measurements. A remarkably fruitful avenue in that regard has been the use of Genetic Algorithms (GAs) (Goldberg, 1989) and other nature-inspired techniques such as the Artificial Bee Colony (ABC) algorithm (Karaboga, 2005). This is because such heuristic algorithms facilitate an almost exhaustive search[2]; and they can be applied to complex (nonlinear, multi-dimensional) optimization problems—including inverse scattering (Fan et al., 2002)—with ease.

In recent years, and pertinent to the present study, Rabinovich et al. (2007) proposed a combined XFEM-GA approach for single or multiple scatterers with regular geometry (i.e., a straight line crack, a circle, or an ellipse). The same approach of combining XFEM with heuristic minimization algorithms continued to the present day with various algorithmic advances and some experimental validation (Chatzi et al., 2011; Rabinovich et al., 2009; Sun et al., 2013; Waisman et al., 2010).

While successful, the aforementioned XFEM-GA algorithms entail a large number of forward solves in order to converge on the optimum values; and the computational cost exponentially increases with the number of updating parameters. Moreover, existing literature either has only dealt with simple inclusions shapes, or elasto-static data. An alternative approach based a combination of a classical gradient-based minimization method and elasto-dynamic XFEM had been pursued by Jung and Taciroglu, since the inception of this present dissertation in early 2010 (Jung, 2011)[3].

[2]Heuristic algorithms such as GAs and ABC algorithms are computationally costly, but they typically yield *all* of the minimizers.

[3]This research has culminated in several archival publications to date—namely, Jung et al.

The outline and notable features of the proposed approach can be summarized as follows:

- Forward wave propagation problem is solved using a dynamic XFEM framework wherein the geometry and location of arbitrarily shaped scatterers (e.g., cracks, voids, or inclusions) are represented with cubic splines, which is unique to the present study. The forward solver can accommodate any instrumentation plan, excitation type (single/multiple, broadband/harmonic, etc.), specimen geometry, and material heterogeneities and anisotropy.

- The inverse problem is solved using a gradient-based minimization method that is enhanced with a divide-alternate-and-conquer algorithm that can be used to localize multiple scatterers and to identify their shapes. The said algorithms are also unique to the present study, and provide robustness with regard to local minimizers.

- Parameters that define the cubic splines serve as the updating parameters, which are adaptively increased to reduce the computational cost and to improve the overall robustness of the proposed approach.

- While it will not be specifically pursued here, the proposed approach is highly amenable to parallel programming.

1.3 Organization of this thesis document

The remainder of this thesis is organized as follows: Chapter 2 presents the dynamic XFEM formulation for a crack, a void, and an inclusion, as well as the cubic spline modeling for arbitrary geometries. These ingredients collectively serve as the forward solver for the shape localization and identification problem. Chapter 3 provides the description of the gradient-based optimization method,

(2013) and Jung and Taciroglu (2014)—which form a part of this dissertation.

and the robust search algorithms that are used in combination with it—*viz.*, a divide-alternate-and-conquer strategy—to identify multiple scatterers. Chapter 4 presents several numerical experiments that are carried out to verify the proposed methodology and to assess its performance. Concluding remarks are presented in Chapter 5.

CHAPTER 2

Dynamic XFEM Endowed with Spline-Based Interfaces for Solving the Forward Problem

2.1 The governing equations for wave propagation in the time domain

We consider an inverse scattering problem in which a linear elastic heterogeneous host medium occupies the open set $\Omega \subset \mathbb{R}^2$ bounded by $\mathbf{\Gamma}$, as shown in Figure 2.1,

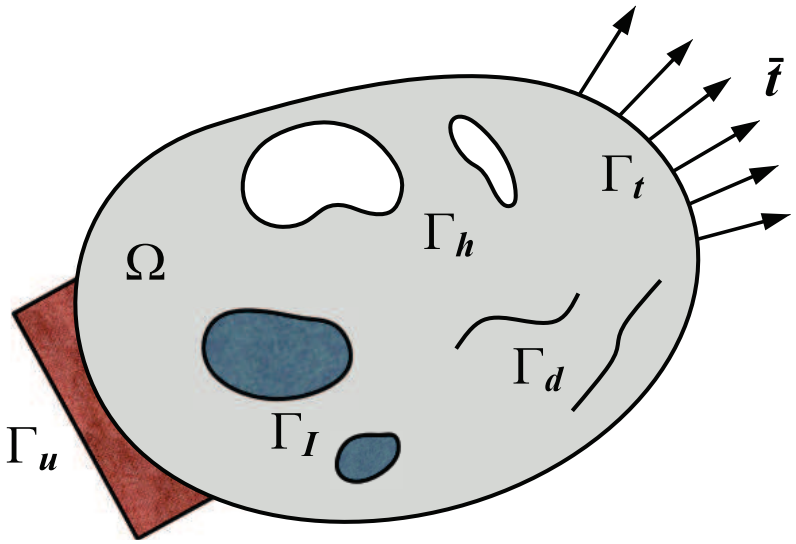

Figure 2.1: Initial-boundary value problem with cracks, voids, and inclusions embedded within an elastic medium.

such that

$$\begin{aligned} \boldsymbol{\Gamma}_u \cup \boldsymbol{\Gamma}_t \cup (\boldsymbol{\Gamma}_d,\ \boldsymbol{\Gamma}_h \text{ or } \boldsymbol{\Gamma}_I) &= \boldsymbol{\Gamma}, \\ \boldsymbol{\Gamma}_u \cap \boldsymbol{\Gamma}_t &= \emptyset, \\ \boldsymbol{\Gamma}_u \cap (\boldsymbol{\Gamma}_d,\ \boldsymbol{\Gamma}_h \text{ or } \boldsymbol{\Gamma}_I) &= \emptyset, \\ \boldsymbol{\Gamma}_t \cap (\boldsymbol{\Gamma}_d,\ \boldsymbol{\Gamma}_h \text{ or } \boldsymbol{\Gamma}_I) &= \emptyset, \end{aligned} \tag{2.1}$$

where $\boldsymbol{\Gamma}_u$ and $\boldsymbol{\Gamma}_t$ denote the specified displacement and traction along the outer boundary of Ω, respectively; $\boldsymbol{\Gamma}_d$, the crack surfaces; $\boldsymbol{\Gamma}_h$, the void surfaces; and $\boldsymbol{\Gamma}_I$, the material interfaces of inclusions.

The strong form of the governing equations describing elastic wave motion and the initial conditions are

$$\boldsymbol{\nabla} \cdot \boldsymbol{\sigma} + \boldsymbol{b} = \rho \ddot{\boldsymbol{u}} \quad \text{in } \Omega, \tag{2.2}$$

$$\boldsymbol{u}(\boldsymbol{x}, 0) = 0 \quad \text{in } \Omega, \tag{2.3}$$

$$\dot{\boldsymbol{u}}(\boldsymbol{x}, 0) = 0 \quad \text{in } \Omega, \tag{2.4}$$

where $\nabla\cdot$ denotes the divergence operator; $\boldsymbol{\sigma} := \boldsymbol{\sigma}(\boldsymbol{x}, t)$, the Cauchy stress tensor; $\boldsymbol{x}$, the spatial position; t, time; $\boldsymbol{b} := \boldsymbol{b}(\boldsymbol{x}, t)$, the body force per unit volume; $\rho := \rho(\boldsymbol{x})$, the mass density; $\boldsymbol{u} := [u_1(\boldsymbol{x}, t)\ u_2(\boldsymbol{x}, t)]^T$, the displacement vector; and $\dot{(\,)}$ and $\ddot{(\,)}$ indicate the first and second partial derivatives of the state variables with respect to time t, respectively. The associated boundary conditions are given as

$$\boldsymbol{u} = \bar{\boldsymbol{u}} \quad \text{on } \boldsymbol{\Gamma}_u, \tag{2.5}$$

$$\boldsymbol{\sigma} \cdot \boldsymbol{n} = \bar{\boldsymbol{t}} \quad \text{on } \boldsymbol{\Gamma}_t, \tag{2.6}$$

$$\boldsymbol{\sigma} \cdot \boldsymbol{n} = 0 \quad \text{on } \boldsymbol{\Gamma}_d \text{ and/or } \boldsymbol{\Gamma}_h, \tag{2.7}$$

$$[|\boldsymbol{\sigma} \cdot \boldsymbol{n}|] = 0 \quad \text{on } \boldsymbol{\Gamma}_I, \tag{2.8}$$

where $\boldsymbol{n}$ is the outward unit vector normal on the boundary of Ω; $\bar{\boldsymbol{u}}$ and $\bar{\boldsymbol{t}}$ are, respectively, the prescribed displacements and tractions on $\boldsymbol{\Gamma}_u$ and $\boldsymbol{\Gamma}_t$; the displacement and traction boundary conditions are, respectively, held along $\boldsymbol{\Gamma}_u$ and

$\boldsymbol{\Gamma}_t$; the traction-free conditions are imposed on $\boldsymbol{\Gamma}_d$ and $\boldsymbol{\Gamma}_h$; and the interface traction continuity conditions are assumed over $\boldsymbol{\Gamma}_I$.

The constitutive relationships for linear elastic media are defined as

$$\boldsymbol{\sigma} = \quad \boldsymbol{C}\boldsymbol{\epsilon}, \tag{2.9}$$

$$\boldsymbol{\epsilon} = \quad \tfrac{1}{2}\left(\nabla \boldsymbol{u} + \nabla \boldsymbol{u}^T\right), \tag{2.10}$$

where $\boldsymbol{C}$ is the material elasticity tensor; $\boldsymbol{\epsilon}$ is the strain tensor; and ∇ is the gradient operator.

2.2 The weak form of the governing equations and its spatial discretization

The weak form corresponding to the governing wave equation (2.2) is

$$\int_\Omega (\boldsymbol{\nabla} \cdot \boldsymbol{\sigma}) \cdot \delta \boldsymbol{u} d\Omega + \int_\Omega \boldsymbol{b} \cdot \delta \boldsymbol{u} d\Omega = \int_\Omega \rho \ddot{\boldsymbol{u}} \cdot \delta \boldsymbol{u} d\Omega, \tag{2.11}$$

where $\delta \boldsymbol{u}$ are the test functions that belong to $\mathcal{H}^1(\Omega)$—i.e., the first-order Sobolev-space continuous functions—except for the essential boundary $\boldsymbol{\Gamma}_u$ in Ω.

Using integration by parts and the divergence theorem, the discretized weak form of linear elastodynamics for $\boldsymbol{u}^h \in \mathcal{U}^h$ and $\delta \boldsymbol{u}^h \in \mathcal{V}^h$ leads to

$$\int_\Omega \rho \ddot{\boldsymbol{u}}^h \cdot \delta \boldsymbol{u}^h d\Omega + \int_\Omega \boldsymbol{\sigma} : \delta \epsilon^h d\Omega = \int_{\Gamma_t} \bar{\boldsymbol{t}} \cdot \delta \boldsymbol{u}^h d\Gamma + \int_\Omega \boldsymbol{b} \cdot \delta \boldsymbol{u}^h d\Omega, \quad \forall \delta \boldsymbol{u}^h \in \mathcal{V}^h \tag{2.12}$$

with

$$\mathcal{U}^h = \{\boldsymbol{u}^h | \boldsymbol{u}^h \in (\mathcal{H}^{1h})^d, \boldsymbol{u}^h = \bar{\boldsymbol{u}}^h \ \text{ on } \ \boldsymbol{\Gamma}_u\}, \tag{2.13}$$

$$\mathcal{V}^h = \{\delta \boldsymbol{u}^h | \delta \boldsymbol{u}^h \in (\mathcal{H}^{1h})^d, \delta \boldsymbol{u}^h = 0 \ \text{ on } \ \boldsymbol{\Gamma}_u\}, \tag{2.14}$$

where $\mathcal{H}^{1h} \subseteq \mathcal{H}^1$ denote finite dimensional Hilbert spaces consisting of the shape functions; $\boldsymbol{u}^h$ and $\delta \boldsymbol{u}^h$ are the finite element approximations of the trial and test functions.

2.3 Time integration of the discretized wave equations

From the weak form of Eq. (2.12) that is discretized using Eq. (2.31), we can obtain the time-dependent discrete form of the equations of motion, as in

$$\mathrm{M}\ddot{\boldsymbol{s}} + \mathrm{K}\boldsymbol{s} = \mathbf{f}, \tag{2.15}$$

where M and K are, respectively, the global mass and stiffness matrices; $\boldsymbol{s}$ and $\ddot{\boldsymbol{s}}$ denote, respectively, the displacement vector of the nodal degrees of freedom and its second time derivative; and $\mathbf{f}$ is the time-dependent force vector. M, K, $\boldsymbol{s}$ and $\mathbf{f}$ for each element e are defined as

$$\mathrm{M}^{\boldsymbol{e}} = \begin{bmatrix} \mathrm{M}^{uu} & \mathrm{M}^{ua} \\ \mathrm{M}^{au} & \mathrm{M}^{aa} \end{bmatrix}, \mathrm{K}^{\boldsymbol{e}} = \begin{bmatrix} \mathrm{K}^{uu} & \mathrm{K}^{ua} \\ \mathrm{K}^{au} & \mathrm{K}^{aa} \end{bmatrix}, \tag{2.16}$$

$$\boldsymbol{s}^{e} = \left\{ \boldsymbol{u}_{1x}, \boldsymbol{u}_{1y}, \cdots, \boldsymbol{u}_{4x}, \boldsymbol{u}_{4y}, \boldsymbol{a}_{1x}, \boldsymbol{a}_{1y}, \cdots, \boldsymbol{a}_{4x}, \boldsymbol{a}_{4y} \right\}^{T}, \tag{2.17}$$

$$\mathrm{f}^{\boldsymbol{e}} = \left\{ \begin{array}{cc} \mathbf{f}^{u}, & \mathbf{f}^{a} \end{array} \right\}^{T}, \tag{2.18}$$

where the mass (or stiffness) components M^{uu} (or K^{uu}), M^{ua} (or K^{ua}) and M^{aa} (or K^{aa}) are associated with the classical finite element approximation, and the coupled and the enriched approximation of XFEM, respectively, defined as

$$\mathrm{M}^{pq} = \int_{\Omega^e} \rho N_p^T N_q d\Omega \qquad (p,\ q = u,\ a), \tag{2.19}$$

$$\mathrm{K}^{pq} = \int_{\Omega^e} \mathrm{B}_p^T \boldsymbol{C} \mathrm{B}_q d\Omega \qquad (p,\ q = u,\ a), \tag{2.20}$$

where N_u and N_a are the standard and the enrichment shape functions for a four-node quadrilateral finite element, respectively. These matrices are defined as

$$\mathrm{N}_u = \begin{bmatrix} N_1 & 0 & N_2 & 0 & N_3 & 0 & N_4 & 0 \\ 0 & N_1 & 0 & N_2 & 0 & N_3 & 0 & N_4 \end{bmatrix}, \tag{2.21}$$

$$\mathrm{N}_a = \begin{bmatrix} N_1\varphi^{\text{shift}} & 0 & N_2\varphi^{\text{shift}} & 0 & N_3\varphi^{\text{shift}} & 0 & N_4\varphi^{\text{shift}} & 0 \\ 0 & N_1\varphi^{\text{shift}} & 0 & N_2\varphi^{\text{shift}} & 0 & N_3\varphi^{\text{shift}} & 0 & N_4\varphi^{\text{shift}} \end{bmatrix}. \tag{2.22}$$

B_u and B_a are the shape function derivative matrices, given by

$$\mathrm{B}_u = \begin{bmatrix} N_{1,x} & 0 & N_{2,x} & 0 & N_{3,x} & 0 & N_{4,x} & 0 \\ 0 & N_{1,y} & 0 & N_{2,y} & 0 & N_{3,y} & 0 & N_{4,y} \\ N_{1,y} & N_{1,x} & N_{2,y} & N_{2,x} & N_{3,y} & N_{3,x} & N_{4,y} & N_{4,x} \end{bmatrix}, \tag{2.23}$$

$$\mathrm{B}_a = \begin{bmatrix} (N_1\varphi^{\text{shift}})_{,x} & 0 & \cdots & (N_4\varphi^{\text{shift}})_{,x} & 0 \\ 0 & (N_1\varphi^{\text{shift}})_{,y} & \cdots & 0 & (N_4\varphi^{\text{shift}})_{,y} \\ (N_1\varphi^{\text{shift}})_{,y} & (N_1\varphi^{\text{shift}})_{,x} & \cdots & (N_4\varphi^{\text{shift}})_{,y} & (N_4\varphi^{\text{shift}})_{,x} \end{bmatrix}. \tag{2.24}$$

Finally, $\mathbf{f}^u$ and $\mathbf{f}^a$ are time-dependent applied force vectors for the classical and enrichment components of the displacement approximation, given by

$$\mathbf{f}^u = \int_{\Gamma_t} (N_u)^T \bar{\boldsymbol{t}}\, d\Gamma + \int_\Omega (N_u)^T \boldsymbol{b}\, d\Omega, \tag{2.25}$$

$$\mathbf{f}^a = \int_{\Gamma_t} (N_a)^T \bar{\boldsymbol{t}}\, d\Gamma + \int_\Omega (N_a)^T \boldsymbol{b}\, d\Omega. \tag{2.26}$$

Note that the standard mass and stiffness matrices (M^{uu} and K^{uu}), and the conventional FE shape and shape-derivative functions (N_u and B_u) are used in all elements except the enriched ones.

The Newmark time integration scheme is adopted to solve the discrete form of Eq. (2.15) at the n-th time step, which is given by

$$\mathrm{M}\ddot{\boldsymbol{s}}_n + \mathrm{K}\boldsymbol{s}_n = \mathbf{f}_n. \tag{2.27}$$

The discrete velocities and displacements are approximated at the n-th time step with

$$\begin{aligned} \dot{\boldsymbol{s}}_n &= \dot{\boldsymbol{s}}_{n-1} + (1-\alpha)\Delta t \ddot{\boldsymbol{s}}_{n-1} + \alpha \Delta t \ddot{\boldsymbol{s}}_n, \\ \boldsymbol{s}_n &= \boldsymbol{s}_{n-1} + \Delta t \dot{\boldsymbol{s}}_{n-1} + (1-2\beta)\frac{\Delta t^2}{2}\ddot{\boldsymbol{s}}_{n-1} + \beta \Delta t^2 \ddot{\boldsymbol{s}}_n\,. \end{aligned} \tag{2.28}$$

Substitution of these into Eq. (2.27) yields the discrete system of equations

$$\left(\mathrm{M} + \beta \Delta t^2 \mathrm{K}\right) \ddot{\boldsymbol{s}}_n = \mathbf{f}_n - \mathrm{K}\left(\boldsymbol{s}_{n-1} + \Delta t \dot{\boldsymbol{s}}_{n-1} + (1-2\beta)\frac{\Delta t^2}{2}\ddot{\boldsymbol{s}}_{n-1}\right). \tag{2.29}$$

After solving for $\ddot{\boldsymbol{s}}_n$, the vectors $\dot{\boldsymbol{s}}_n$ and $\boldsymbol{s}_n$ are updated using Eq. (2.28). In the present study, we utilize Newmark's implicit time integration scheme ($\alpha = 1/2$ and $\beta = 1/4$), which provides second-order accuracy and unconditional stability.

2.4 The eXtended Finite Element formulation

2.4.1 Standard XFEM

Based on the concept of partition of unity (Melenk and Babuška, 1996), the displacement approximation of the general XFEM is given in the form

$$\boldsymbol{u}^h(\boldsymbol{x}) = \sum_{i \in I} N_i(\boldsymbol{x}) \boldsymbol{u}_i + \sum_{i \in I^\star} N_i^\star(\boldsymbol{x}) \varphi(\boldsymbol{x}) \boldsymbol{a}_i \,. \tag{2.30}$$

The above approximation consists of a classical finite element approximation (indicated by the summation with respect to $i \in I$), and an enriched approximation (indicated by the summation with respect to $i \in I^\star$). In Eq. (2.30), I is the set of all nodes; $I^\star \subset I$ is the set of the nodes with a discontinuity; $N_i(\boldsymbol{x})$ and $N_i^\star(\boldsymbol{x})$ are the finite element shape functions corresponding to the i-th node located at $\boldsymbol{x}_i$; $\boldsymbol{u}_i$ and $\boldsymbol{a}_i$ are the standard and enriched nodal displacements at node i, respectively; and $\varphi(\boldsymbol{x})$ is the local enrichment function associated with the discontinuity. It is noted that $N_i(\boldsymbol{x})$ and $N_i^\star(\boldsymbol{x})$ are not necessarily equal to each other, but generally $N_i(\boldsymbol{x}) = N_i^\star(\boldsymbol{x})$ are used (Belytschko et al., 2009).

If the approximated form—i.e., Eq. (2.30)—is used, then it is difficult to impose essential boundary conditions of $\boldsymbol{u}_i$ on $\boldsymbol{u}^h(\boldsymbol{x}_i)$ because the enrichment terms do not vanish on the enriched nodes—i.e., $\boldsymbol{u}^h(\boldsymbol{x}_i) \neq \boldsymbol{u}_i$. Moreover, additional calculations for evaluating all of the terms in the approximation are required to find the actual displacement value $\boldsymbol{u}^h(\boldsymbol{x}_i)$. To overcome these shortcomings, the shifted—instead of the standard—enrichment functions are used, which were first

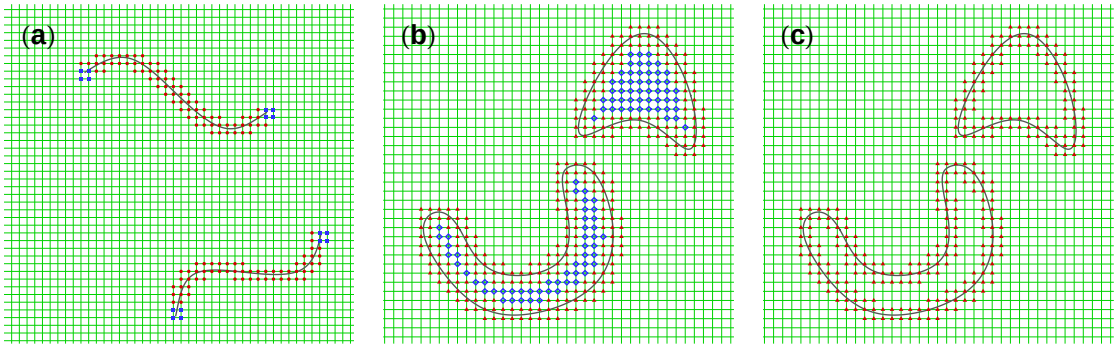

Figure 2.2: Examples of enriched nodal sets for (a) curved cracks, (b) arbitrarily shaped voids and (c) arbitrarily shaped inclusions, marked by solid lines (■: enriched nodes near crack tips, •: enriched nodes near crack faces, ▲: enriched nodes near voids or inclusions, ♢: nodes corresponding to zero/void degrees of freedom).

suggested by Belytschko et al. (2001) as

$$\boldsymbol{u}^h(\boldsymbol{x}) = \sum_{i\in I} N_i(\boldsymbol{x})\boldsymbol{u}_i + \sum_{i\in I^\star} N_i^\star(\boldsymbol{x})\varphi_i^{\text{shift}}\boldsymbol{a}_i, \tag{2.31}$$

where $\varphi_i^{\text{shift}} = [\varphi(\boldsymbol{x}) - \varphi(\boldsymbol{x}_i)]$. In the following subsections, we present XFEM approximations with these shifted enrichment functions for different types of scatterer geometries.

2.4.2 XFEM for a general crack

Based on the concept of partition of unity (Melenk and Babuška, 1996), the approximated displacements for general cracks can be decomposed into two parts: (i) a conventional finite element approximation part (denoted by the summation with respect to $i \in I$); and (ii) an enrichment approximation part (respectively, denoted by the summation with respect to $j \in I$, and $k \in I_\Lambda$) (Fries and Be-

lytschko, 2010) as

$$\boldsymbol{u}^h(\boldsymbol{x}) = \sum_{i\in I} N_i(\boldsymbol{x})\boldsymbol{u}_i + \sum_{j\in I_\Gamma} N_j(\boldsymbol{x})\left[\psi_{\text{sign}}(\boldsymbol{x}) - \psi_{\text{sign}}(\boldsymbol{x}_j)\right]\boldsymbol{b}_j + \sum_{k\in I_\Lambda} N_k(\boldsymbol{x})\left(\sum_{\alpha=1}^{4}\left[F_\alpha(\boldsymbol{x}) - F_\alpha(\boldsymbol{x}_k)\right]\boldsymbol{c}_k^\alpha\right). \tag{2.32}$$

Here, I denotes the set of all nodes in the computational domain (including the cracks, voids, and inclusions); I_Γ, the set of the enriched nodes of elements fully cut by the cracks Γ_d (marked with red-filled circles in Figure 2.2(a)); I_Λ, the set of the enriched nodes containing the crack tips (marked with blue-filled squares in Figure 2.2(a)); $N_{(i,\ j \text{ or } k)}(\boldsymbol{x})$, the standard finite element shape functions associated with the $(i,\ j$ or $k)$-th node at the location of $\boldsymbol{x}_{(i,\ j \text{ or } k)}$; $\boldsymbol{u}_i$, the standard nodal displacement vectors at node i; $\boldsymbol{b}_j$ and $\boldsymbol{c}_k^\alpha$, respectively, the enriched nodal displacement vectors involving the discontinuous function $\psi_{\text{sign}}(\boldsymbol{x})$ and the asymptotic crack-tip function $F_\alpha(\boldsymbol{x})$ at node j and k.

The discontinuity in the interior of the cracks is described by means of the signed-distance level set function $\psi_{\text{sign}}(\boldsymbol{x})$ (Figure 2.3), whose value is defined as

$$\psi_{\text{sign}}(\boldsymbol{x}) = \text{sign}(\psi(\boldsymbol{x})) = \begin{cases} -1 & \text{if } \psi(\boldsymbol{x}) < 0 \qquad \text{(below crack path)}, \\ 0 & \text{if } \psi(\boldsymbol{x}) = 0 \qquad \text{(along crack path)}, \\ 1 & \text{if } \psi(\boldsymbol{x}) > 0 \qquad \text{(above crack path)}, \end{cases} \tag{2.33}$$

with

$$\psi(\boldsymbol{x}) = \pm \min \|\boldsymbol{x} - \boldsymbol{x}_{\Gamma_d}\| \qquad \forall \boldsymbol{x}_{\Gamma_d} \in \Gamma_d \qquad \forall \boldsymbol{x} \in \Omega, \tag{2.34}$$

where $\|\cdot\|$ denotes the Euclidean norm.

The structural behavior around the crack tips in isotropic elastic media can be characterized by using crack-tip enrichment functions which are defined by the asymptotic displacements (Fleming et al., 1997) below,

$$[F_1,\ F_2,\ F_3,\ F_4] = \sqrt{r}\left[\ \sin\frac{\theta}{2},\ \ \cos\frac{\theta}{2},\ \ \sin\theta\sin\frac{\theta}{2},\ \ \sin\theta\cos\frac{\theta}{2}\right], \tag{2.35}$$

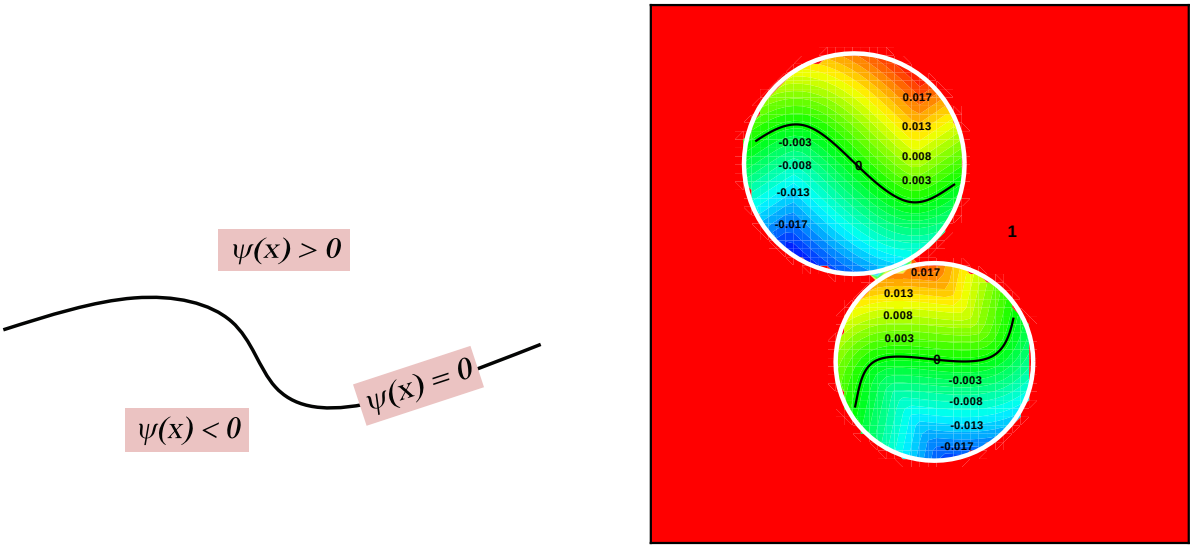

Figure 2.3: Construction of the level set functions (ψ) (left). The contour plot of ψ within search areas (white circles) for curved cracks that are marked by the solid lines (right).

where r and θ are the polar coordinates in the local crack-tip coordinate system as shown in Figure 2.4.

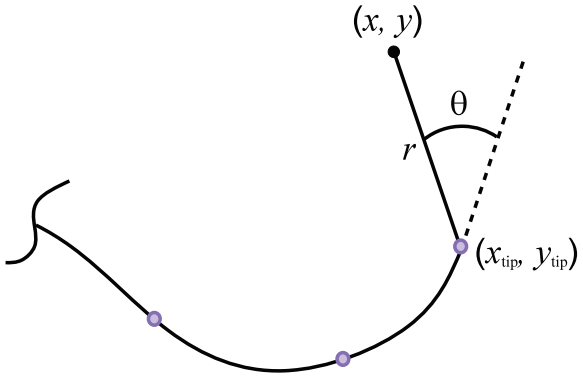

Figure 2.4: Coordinate system (r, θ) for a crack tip.

2.4.3 XFEM for a crack located at a material interface

For the case of a bi-material crack when the crack is located at the interface between materials (see Figure 2.2(b)), the XFEM approximation is defined as follows

$$\boldsymbol{u}^h(\boldsymbol{x}) = \sum_{i\in I} N_i(\boldsymbol{x})\boldsymbol{u}_i + \sum_{j\in I_\Gamma} N_j(\boldsymbol{x})\left[\psi_{\text{sign}}(\boldsymbol{x}) - \psi_{\text{sign}}(\boldsymbol{x}_j)\right]\boldsymbol{b}_j + \sum_{k\in I_\Lambda} N_k(\boldsymbol{x})\left(\sum_{\alpha=1}^{12}\left[F_\alpha(\boldsymbol{x}) - F_\alpha(\boldsymbol{x}_k)\right]\boldsymbol{c}_k^\alpha\right), \tag{2.36}$$

where only the crack-tip enrichment portion of Eq. (2.32) that corresponds to the general crack is replaced. The set of crack-tip enrichment functions are those introduced by Sukumar et al. (2004), and are given as follows

$$\begin{aligned}[F_\alpha(r,\,\theta,\,\varepsilon),\ \alpha = 1\text{-}12] = \sqrt{r}\Bigg[\ & \cos(\varepsilon\,\log r)e^{-\varepsilon\theta}\sin\frac{\theta}{2},\quad \cos(\varepsilon\,\log r)e^{-\varepsilon\theta}\cos\frac{\theta}{2},\\ & \cos(\varepsilon\,\log r)e^{\varepsilon\theta}\sin\frac{\theta}{2},\quad \cos(\varepsilon\,\log r)e^{\varepsilon\theta}\cos\frac{\theta}{2},\\ & \cos(\varepsilon\,\log r)e^{\varepsilon\theta}\sin\theta\sin\frac{\theta}{2},\quad \cos(\varepsilon\,\log r)e^{\varepsilon\theta}\sin\theta\cos\frac{\theta}{2},\\ & \sin(\varepsilon\,\log r)e^{-\varepsilon\theta}\sin\frac{\theta}{2},\quad \sin(\varepsilon\,\log r)e^{-\varepsilon\theta}\cos\frac{\theta}{2},\\ & \sin(\varepsilon\,\log r)e^{\varepsilon\theta}\sin\frac{\theta}{2},\quad \sin(\varepsilon\,\log r)e^{\varepsilon\theta}\cos\frac{\theta}{2},\\ & \sin(\varepsilon\,\log r)e^{\varepsilon\theta}\sin\theta\sin\frac{\theta}{2},\quad \sin(\varepsilon\,\log r)e^{\varepsilon\theta}\sin\theta\cos\frac{\theta}{2}\Bigg],\end{aligned} \tag{2.37}$$

where ε is the bi-material constant, given by

$$\varepsilon = \frac{1}{2\pi}\log\left(\frac{1-\beta}{1+\beta}\right), \tag{2.38}$$

and β is the second Dundurs parameter (Dundurs, 1969) given by

$$\beta = \frac{\mu_1(\kappa_2-1) - \mu_2(\kappa_1-1)}{\mu_1(\kappa_2+1) + \mu_2(\kappa_1+1)}. \tag{2.39}$$

Here, μ_i and κ_i denote the shear modulus and the "Kolosov" constant for the i-th material ($i = 1$, or $i = 2$), respectively. The Kosolov constant is given in terms of

Poisson's ratio as

$$\kappa_i = \begin{cases} \dfrac{3-\nu_i}{1+\nu_i} & \text{for plane stress,} \\ 3-4\nu_i & \text{for plane strain.} \end{cases} \tag{2.40}$$

2.4.4 XFEM for a void

The XFEM approximation for voids can carried out by using an enrichment function $V(\boldsymbol{x})$ (Sukumar et al., 2001) given by

$$\boldsymbol{u}^h(\boldsymbol{x}) = V(\boldsymbol{x}) \sum_{i \in I} N_i(\boldsymbol{x}) \boldsymbol{u}_i, \tag{2.41}$$

where

$$V(\boldsymbol{x}) = \begin{cases} 1 & \text{if } \boldsymbol{x} \in \Omega, \\ 0 & \text{if } \boldsymbol{x} \notin \Omega. \end{cases} \tag{2.42}$$

As illustrated in Figure 2.2(b), the nodes at the elements enclosing the internal boundary of voids (▲) have $V(\boldsymbol{x}) = 1$, while $V(\boldsymbol{x}) = 0$ is assumed at the nodes of the elements inside the voids (◇). Hence, the XFEM solution can be obtained simply by numerical integration of element matrices in the same way as in conventional FEM only over Ω.

2.4.5 XFEM for a inclusion

For the modeling the inclusions, the XFEM displacement approximation function suggested by Moës et al. (2003) can be used, which employs a level set function ζ, as in,

$$\boldsymbol{u}^h(\boldsymbol{x}) = \sum_{i \in I} N_i(\boldsymbol{x}) \boldsymbol{u}_i + \sum_{j \in I_\Gamma} N_j(\boldsymbol{x}) \left[\sum_{i \in I} N_i(\boldsymbol{x}) \left| \zeta_i \right| - \left| \sum_{i \in I} N_i(\boldsymbol{x}) \zeta_i \right| \right] \boldsymbol{a}_j, \tag{2.43}$$

where

$$\zeta(\boldsymbol{x}) = \pm \min \left\| \boldsymbol{x} - \boldsymbol{x}_{\Gamma_I} \right\| \qquad \forall \boldsymbol{x}_{\Gamma_I} \in \Gamma_I \qquad \forall \boldsymbol{x} \in \Omega. \tag{2.44}$$

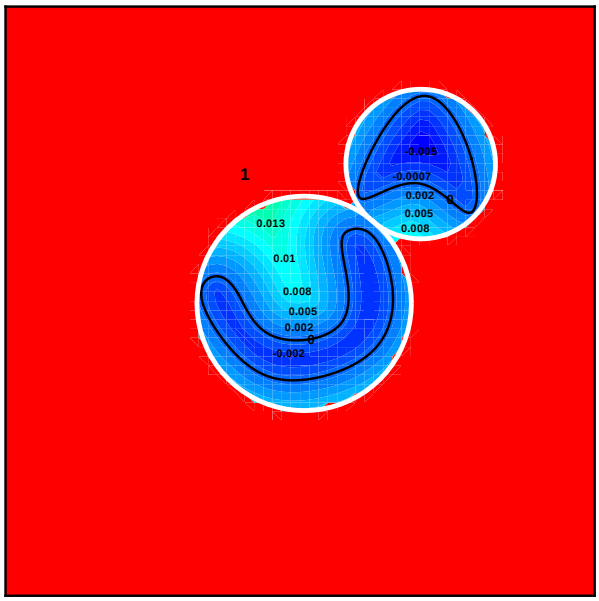

Figure 2.5: The contour plot of ζ within search areas (white circles) for inclusions, the interface of which is shown by solid lines. Note that for voids, the level set function ζ is used as well, in order to distinguish the nodes inside and outside the voids.

The level set function ζ (see, Figures 2.2.c, and 2.5) plays a crucial role in the representation of closed geometries (i.e., inclusions and voids). As this is closely related to the discussion of parametric cubic splines, the determination of the sign and magnitude of ζ is deferred to §2.5.3 and §2.5.4.

2.5 Parametric cubic spline methods

In this section, we briefly explain how to construct the open/closed geometries of arbitrarily shaped scatterers (cracks/voids or inclusions) using cubic splines[1]. In particular, the parametric cubic spline method allows closed geometries to be constructed with a relatively few number of control points and shape parameters, which is a highly favorable attribute for the optimization problems at hand.

[1]This formulation may also be found in (Jung and Taciroglu, 2014).

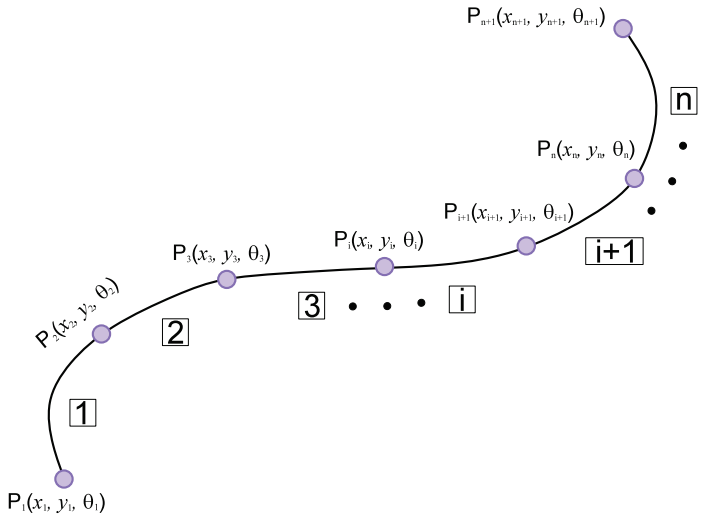

Figure 2.6: Representation of an open curve geometry with cubic splines.

2.5.1 Representation of open curves

Cubic splines are used for representing curved cracks with a minimal number of discrete control points/segments. As shown in Figure 2.6, each discrete curve segment (marked with the numbered squares) is made up of control points (marked with filled circles). Each control point bears three shape parameters—*viz.*, the x and y coordinates and the curve slopes (θ). For the generic i-th curve segment, the cubic interpolating spline function is given by

$$y = a_i x^3 + b_i x^2 + c_i x + d_i, \tag{2.45}$$

where the coefficients are determined by

$$\begin{Bmatrix} a_i \\ b_i \\ c_i \\ d_i \end{Bmatrix} = \begin{bmatrix} x_i^3 & x_i^2 & x_i & 1 \\ x_{i+1}^3 & x_{i+1}^2 & x_{i+1} & 1 \\ 3x_i^2 & 2x_i & 1 & 0 \\ 3x_{i+1}^3 & 2x_{i+1}^3 & 1 & 0 \end{bmatrix}^{-1} \begin{Bmatrix} y_i \\ y_{i+1} \\ \theta_i \\ \theta_{i+1} \end{Bmatrix}. \tag{2.46}$$

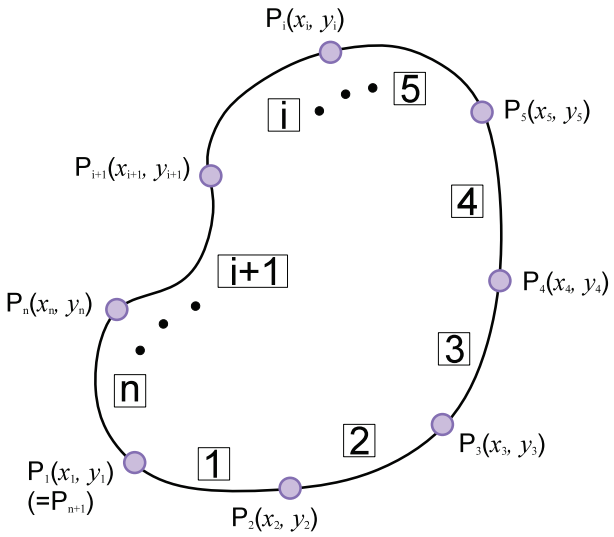

Figure 2.7: Representation of a closed-curve geometry with cubic splines.

2.5.2 Representation of closed curves

Parametric cubic splines are used for the modeling the boundary of an arbitrarily shaped void or inclusion. This approach offers the following two advantages: (i) the variables x and y are uncoupled from each other (through the use of a curvilinear coordinate system), which makes it easier to construct complicated geometries compared to conventional cubic spline methods; (ii) each individual control point of the cubic spline segments has two shape parameters, $x,\ y$ coordinates, excluding θ.

The parametric cubic spline functions are defined with respect to an independent variable $s \in [0,\ 1]$ for x_i and y_i along the i-th curve segment as

$$\begin{aligned} x_i(s) &= a_{x_i}(s-s_0)^3 + b_{x_i}(s-s_0)^2 + c_{x_i}(s-s_0) + d_{x_i}, \\ y_i(s) &= a_{y_i}(s-s_0)^3 + b_{y_i}(s-s_0)^2 + c_{y_i}(s-s_0) + d_{y_i}, \end{aligned} \tag{2.47}$$

where s is equally spaced by $(1/n)$ over $s \in [0,\ 1]$ for simplification; s_0 indicates the value of s at the starting point of each segment; n is the total number of control points. In the closed-loop case (see, Figure 2.7), the $(n+1)^{\text{th}}$ control point

is added in the sequence (i.e., $i = 1,\ 2,\ \ldots,\ n,\ 1$), and $P_{n+1} = P_1$ wherein P_i denotes x_i and y_i in each set of cubic spline functions, respectively. The coefficients corresponding to the cubic spline functions $x_i(s)$ and $y_i(s)$ are given by,

$$\begin{aligned} a_{P_i} &= (P''_{i+1} - P''_i)/6h, \\ b_{P_i} &= P''_i/2, \\ c_{P_i} &= (P_{i+1} - P_i)/h - P''_{i+1}h/6 - P''_i h/3, \\ d_{P_i} &= P_i, \end{aligned} \tag{2.48}$$

where h is the spacing between segments, which is chosen as $h = 1/n$ for convenience. Also, the second derivatives P''_i is determined by solving the following $(n+1) \times (n+1)$ matrix

$$\begin{bmatrix} 2 & 1 & 0 & \cdots & 1 & 2 \\ 1 & 4 & 1 & \cdots & 0 & 0 \\ 0 & 1 & 4 & 1 & \cdots & 0 \\ \vdots & \vdots & \ddots & \ddots & \ddots & \vdots \\ 0 & 0 & \cdots & 1 & 4 & 1 \\ 1 & 0 & \cdots & 0 & 0 & -1 \end{bmatrix} \begin{Bmatrix} P''_1 \\ P''_2 \\ P''_3 \\ \vdots \\ P''_m \\ p''_{m+1} \end{Bmatrix} = \frac{6}{h^2} \begin{Bmatrix} P_2 - P_1 - P_{m+1} + P_m \\ P_3 - 2P_2 + P_1 \\ P_4 - 2P_3 + P_2 \\ \vdots \\ P_{m+1} - 2P_m + P_{m-1} \\ 0 \end{Bmatrix} \tag{2.49}$$

Here, the sub-matrix for rows $i = 2$ to m takes a tridiagonal form.

2.5.3 Determination of the sign of the level set function ζ

In order to determine the sign (+ or −) of the level set function ζ, which differentiates between the outside and inside of voids/inclusions with closed curves, we use the modified crossing number method. In the conventional crossing number method, the number of times that a ray—drawn from a point, previously known to be either inside or outside of a closed shape, to a target point—crosses the boundaries of the geometry is counted. After that, from the total crossing number, the sign at the target location is determined. if the crossing number is even

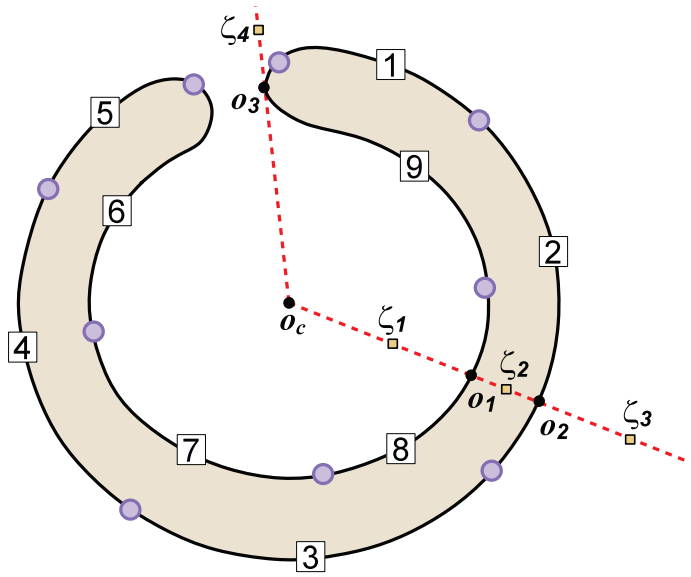

Figure 2.8: An illustration of the modified ray-crossing method for determining the sign of the level set function ζ: purple-filled circles are the control points; numbered squares mark each spline segment between the control points; $\boldsymbol{o}_c$ are the centroid of the geometry; ζ_{1-4} are points along the search line (red-dashed line) at the inside or outside of the geometry; $\boldsymbol{o}_{1-3}$ are the intersection points between the curve segments and the search ray.

(or odd), then the target point is on the same (or opposite) side of the geometry. However, in this approach, we must recognize *a priori* that the given target point's location is either inside or outside the geometry. Hence, a novel *modified* crossing number method is proposed herein, making up for the weakness of the conventional approach, as well as localizing the calculation area near the object.

Figure 2.8, as an example, illustrates how to determine the signs at the points ζ_{1-3} located in the inside or outside of the geometry, which takes the following steps:

i. Set the centroid $\boldsymbol{o}_c$ of the closed geometry from the given information—i.e., control points (purple-filled circles) and cubic curve segments (numbered

Table 2.1: Determining the sign at points ζ_{1-3}.

	ζ_1	ζ_2	ζ_3
$\overline{\boldsymbol{o}_c\zeta_i} - \overline{\boldsymbol{o}_c\boldsymbol{o}_1}$	$-$	$+$	$+$
$\overline{\boldsymbol{o}_c\zeta_i} - \overline{\boldsymbol{o}_c\boldsymbol{o}_2}$	$-$	$-$	$+$
sign	$+$	$-$	$+$

squares).

ii. Draw a ray passing through each target point in question (here, ζ_{1-3}).

iii. Calculate the distances from $\boldsymbol{o}_c$ to ζ_{1-3} and from $\boldsymbol{o}_c$ to each intersection point ($\boldsymbol{o}_1$ and $\boldsymbol{o}_2$) between the ray (red-dashed line) and the cubic curve segments (2 and 8).

iv. Record the signs at ζ_{1-3} (see, Table 2.1), based on the distances from $\boldsymbol{o}_c$ to ζ_{1-3} against $\overline{\boldsymbol{o}_c\boldsymbol{o}_1}$ and $\overline{\boldsymbol{o}_c\boldsymbol{o}_2}$, respectively (e.g., for $\overline{\boldsymbol{o}_c\boldsymbol{o}_1}$, $\zeta_1 < 0 : \overline{\boldsymbol{o}_c\zeta_1} - \overline{\boldsymbol{o}_c\boldsymbol{o}_1}$; $\zeta_{2,\,3} > 0 : \overline{\boldsymbol{o}_c\zeta_{2,\,3}} - \overline{\boldsymbol{o}_c\boldsymbol{o}_1}$).

v. Multiply the signs recorded at ζ_{1-3}, i.e., $\text{sign}(\zeta_i) = \text{sign}(\overline{\boldsymbol{o}_c\zeta_i} - \overline{\boldsymbol{o}_c\boldsymbol{o}_1}) \times \text{sign}(\overline{\boldsymbol{o}_c\zeta_i} - \overline{\boldsymbol{o}_c\boldsymbol{o}_2})$ at $\zeta_i,\ i = 1,\ 2,\ 3$.

It is expedient to note here that (i) the crossing number is not counted exceptively as in the case of ζ_4, wherein the ray goes through the tangent point $\boldsymbol{o}_3$ lying on the curve segment 9; and (ii) the centroid $\boldsymbol{o}_c$ is assumed not to be situated on the boundary of the object, which can be checked by using the parametric cubic spline functions that represent each curve segment.

Figure 2.9 displays the example of the sign of ζ for arbitrarily shaped geometries using the *modified ray-crossing number method* for which the blue- and white-colored areas correspond to negative and positive ζ values, respectively.

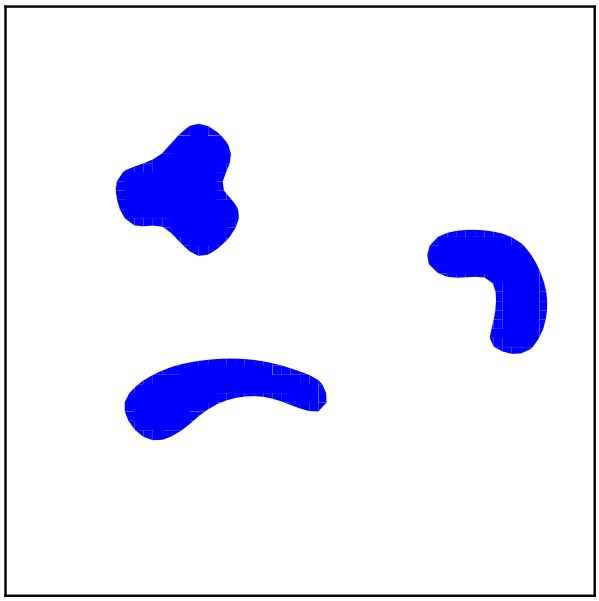

Figure 2.9: A plot of the sign of ζ for arbitrarily shaped geometries using the modified ray-crossing number method; blue-colored/empty areas indicate the negative/positive sign of ζ.

2.5.4 Determination of the magnitude of the level set function ζ

In the present study, the magnitude of the level set function ζ is defined by the shortest distance from any point within the computational domain to the surface of the targeted two-dimensional void/inclusion formed by cubic spline curves.

From §2.5.2, the parametric cubic spline function for any point $(x_{\Gamma_{h/I}},\ y_{\Gamma_{h/I}})$ within a certain curve segment along the boundary of Γ_h or Γ_I is given by

$$\begin{aligned} x_{\Gamma_{h/I}}(s) &= a_x(s-s_0)^3 + b_x(s-s_0)^2 + c_x(s-s_0) + d_x, \\ y_{\Gamma_{h/I}}(s) &= a_y(s-s_0)^3 + b_y(s-s_0)^2 + c_y(s-s_0) + d_y. \end{aligned} \tag{2.50}$$

The distance between $(x_{\Gamma_{h/I}},\ y_{\Gamma_{h/I}})$ and any given point $(x,\ y)$ is

$$d(s) = \sqrt{\left(x - x_{\Gamma_{h/I}}(s)\right)^2 + \left(y - y_{\Gamma_{h/I}}(s)\right)^2}. \tag{2.51}$$

Here, the shortest distance is the optimal value of s obtained by solving the minimization problem of Eq. (2.51). For the minimal $d(s)$, the basic polynomial

equation in terms of s is derived below by substituting Eq. (2.50) into Eq. (2.51), and by differentiating the resultant equation with respect to s (Benowitz and Waisman, 2013).

$$\begin{aligned}
0 =&(3a_x^2 + 3a_y^2)(s - s_0)^5 + (5a_x b_x + 5a_y b_y)(s - s_0)^4 \\
&+ (2b_x^2 + 2b_y^2 + 4a_x c_x + 4a_y c_y)(s - s_0)^3 \\
&+ (-3a_x x - 3a_y y + 3b_x c_x + 3b_y c_y + 3a_x d_x + 3a_y d_y)(s - s_0)^2 \\
&+ (-2x b_x + c_x^2 - 2y b_y + c_y^2 + 2b_x d_x + 2b_y d_y)(s - s_0) \\
&+ (-x c_x + c_x d_x - y c_y + c_y d_y)\,.
\end{aligned} \tag{2.52}$$

Note that the correct answer can be sifted out from the multiple answers in the above equation (2.52) by which the specific range of s in each curve segment is constrained by each s_0 denoting the starting point at curve segments.

CHAPTER 3

A Gradient-based Minimization Method Enhanced with Robust Search Algorithms for Solving the Inverse Problem

3.1 The objective functional

In an identification problem, which is often cast as a minimization problem, the objective functional plays a key role, which converts the morphological difference (size, shape, and location) between the estimated and actual (target) scatterers into a quantitative value. The objective functional adopted here is defined[1] as

$$\mathcal{L}(\boldsymbol{\xi}) = \frac{1}{N_s} \int_0^T \left[\sum_{i=1}^{N_s} \left\| \boldsymbol{u}^{\mathrm{D}}(\boldsymbol{x}_i^s, t; \boldsymbol{\xi}) - \boldsymbol{u}^{\mathrm{M}}(\boldsymbol{x}_i^s, t) \right\| \right] dt, \tag{3.1}$$

where $\boldsymbol{u}^{\mathrm{D}}(\boldsymbol{x}_i^s, t; \boldsymbol{\xi})$ and $\boldsymbol{u}^{\mathrm{M}}(\boldsymbol{x}_i^s, t)$, respectively, indicate the computed and measured wave responses—herein, the displacement of the system variables recorded at the i-th sensor's location $\boldsymbol{x}_i^s$—corresponding to the estimated and actual scatterers. The term $\boldsymbol{\xi}$ denotes the set of unknown shape parameters; N_s, the number of sensors; T, the observation duration; $\| \cdot \|$, the Euclidean norm of a vector.

It is expedient to note that, in the present study, synthetic $\boldsymbol{u}^{\mathrm{M}}(\boldsymbol{x}, t)$—which are computationally generated via dynamic XFEM—instead of actual experimental measurements will employed for method verification and accuracy assessment.

[1] See, also Jung et al. (2013), and Jung and Taciroglu (2014).

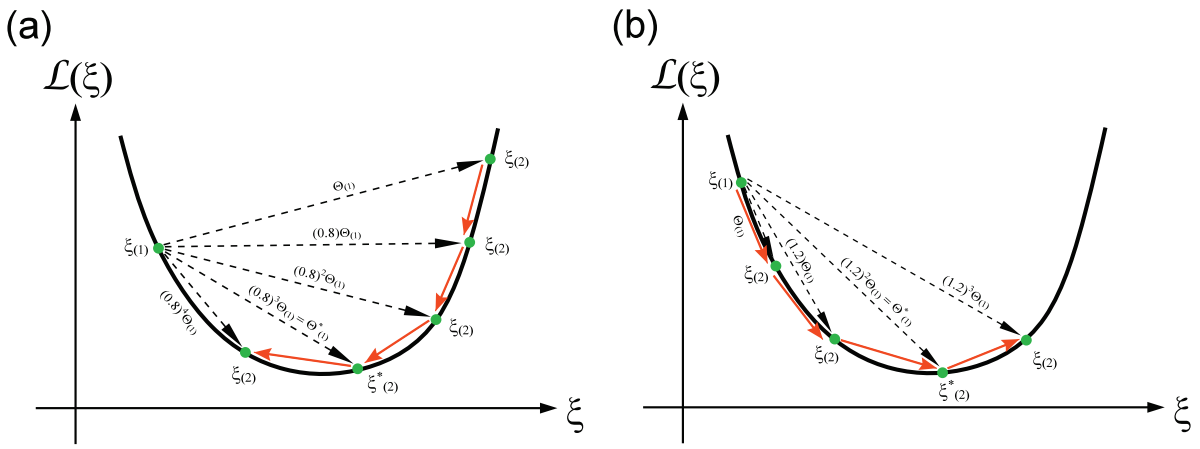

Figure 3.1: Examples of the backtracking line-search for a single shape parameter: (a) for $\mathcal{L}(\boldsymbol{\xi}_{(1)}) \leq \mathcal{L}(\boldsymbol{\xi}_{(2)})$, the step-length is reduced by a factor of 0.8; (b) for $\mathcal{L}(\boldsymbol{\xi}_{(1)}) > \mathcal{L}(\boldsymbol{\xi}_{(2)})$, the step length is increased by a factor of 1.2. In both cases, the computations are repeated until $\mathcal{L}(\boldsymbol{\xi}_{(2)})$ at the next step is greater than $\mathcal{L}(\boldsymbol{\xi}_{(2)})$ at the current step. Here, $\Theta^*_{(1)}$ and $\boldsymbol{\xi}^*_{(2)}$ indicate the optimal step-length and the solution at the current iteration, respectively; and $\boldsymbol{\xi}_{(2)} = \boldsymbol{\xi}_{(1)} + \mathbf{g}\,\Theta_{(1)}$.

3.2 Gradient-based minimization

$\boldsymbol{\xi}^*$ is the global minimum of the objective functional (Eq. 3.1), satisfying the first-order necessary condition $\nabla_{\boldsymbol{\xi}}\mathcal{L}(\boldsymbol{\xi}^*) = 0$ for the optimality. The gradient of the objective functional in this study is approximately established by using a finite difference method as in

$$\nabla_{\xi_j}\mathcal{L} \approx \frac{\mathcal{L}_{\xi_j+\Delta\xi_j} - \mathcal{L}_{\xi_j-\Delta\xi_j}}{2\Delta\xi_j} \tag{3.2}$$

where ξ_j indicates the j-th component of the unknown shape parameter vectors $\boldsymbol{\xi}$.

In order to find the optimal solution (i.e., the global minimizer), we use a gradient-based method, which entails the following procedures:

i. Assign the initial values to the unknown shape parameters $\boldsymbol{\xi}_i$ and step length

Θ_i in which the subscript of (i) indicates the current inverse iteration.

ii. Compute a search direction at the current iteration using the steepest descent method—i.e., the gradient vector $\mathbf{g} = -\nabla_{\boldsymbol{\xi}}\mathcal{L}$.

iii. Find the optimum step size Θ_i^* using the backtracking line-search method, which accelerates the convergence of the optimization.

iv. Update the values of the set of current shape parameters: $\boldsymbol{\xi}_{i+1}^* = \boldsymbol{\xi}_i + \frac{\mathbf{g}}{|\mathbf{g}|}\Theta_i^*$, and then set $\boldsymbol{\xi}_{i+1} = \boldsymbol{\xi}_{i+1}^*$.

v. Iterate the procedures (i) to (iv) until the resulting updated parameters meet the given error tolerances (see Eq. 4.7).

For the case of curved cracks, it should be noted that the gradient of the curve slope (θ) is much less sensitive to the variation of θ than other shape parameters (x and y). Therefore, a weighting factor ($\mathcal{W} = 10^5$) is added into the optimization method as in

$$\theta_{i+1} = \theta_i - \left[\frac{\nabla_{\theta_i}\mathcal{L}}{|\nabla_{\xi_j}\mathcal{L}|}\Theta_i\right]\mathcal{W}. \tag{3.3}$$

In order to find the optimal step-length Θ^* along the search direction at each iteration, a backtracking line-search method is employed (Nocedal and Wright, 2006). For instance, under the assumption that the predicted scatterer is placed near a basin of attraction (a local or global minimizer), for the case of $\mathcal{L}(\boldsymbol{\xi}_{(1)}) \leq \mathcal{L}(\boldsymbol{\xi}_{(2)})$ $\big(= \mathcal{L}(\boldsymbol{\xi}_{(1)} + \mathbf{g}\Theta_{(1)})\big)$, the step-length is reduced at a rate of 0.8 until the following condition is satisfied: $\mathcal{L}(\boldsymbol{\xi}_{(2)})$ by the next step-length is greater than $\mathcal{L}(\boldsymbol{\xi}_{(2)})$ by the current step-length (see, Figure 3.1.a). On the other hand, the step-length is raised by multiplying it by 1.2, for the case of $\mathcal{L}(\boldsymbol{\xi}_{(1)}) > \mathcal{L}(\boldsymbol{\xi}_{(2)})$, until the same condition as that above is fulfilled (see, Figure 3.1.b). Then, the step-length leading to the minimum solution $\boldsymbol{\xi}_{(2)}^*$ is chosen as the optimal step-length $\Theta_{(1)}^*$ at the current iteration.

3.3 A divide-and-conquer strategy for detecting a single scatter

A divide-and-conquer strategy[2] is proposed here to tackle solution multiplicity (local minimizers). In this approach, multiple initial estimates are used in independent inverse problems that all use the same sensor data. In case there is no *a priori* knowledge regarding the location and the geometry of the scatterer, these said initial estimates can be uniformly distributed within the host domain. The premise of this approach is that the majority of the converged solutions will converge to the global (true) minimizer, and that any local minimizer that is inadvertently detected can simply be discarded by comparing the objective function's value there with that at other locations. The said premise was shown to hold by Jung et al. (2013) wherein the method's performance under solution multiplicity due to measurement noise and sensor sparsity were investigated.

Here, the method described by Jung et al. (2013) is extended to have a second phase so that arbitrarily shaped scatterers can be identified efficiently. Similar to the original method, uniformly spaced initial estimates with regular shapes—straight lines for a curved crack or circles for a complex-shaped void and inclusion—are used in the first step. This first phase is intended to only approximately localize the inclusion with a small number of updating parameters. Once the localization is achieved, the last converged geometric representation of the scatterer is switched to a parametric cubic spline set, and a second phase of minimization is carried out to refine the estimated shape. The second step can be repeated by adding control points until a pre-determined objective function norm is achieved (or otherwise, until the solution becomes worse[3]). This two-phase strategy will be described in more detail later with the aid of a flowchart (see,

[2]See, also Jung et al. (2013).

[3]Increasing the number of updating parameters will not necessarily yield a better solution, unless the number of independent sensor measurements are also increased (Hjelmstad, 1996).

Chapter 4).

Remarks: It should be possible to determine the general types and the number of scatters in advance through a relatively crude localization technique (e.g., bulk ultrasonic testing techniques of pitch-catch or pulse-echo (Krautkrämer and Krautkrämer, 1990), which use excitation frequencies in the range of 100 kHz to 15MHz), and this could be used to reduce the number of initial estimates in the divide-and-conquer approach. It is also expedient to note that the divide-and-conquer strategy proposed here is extremely well suited for parallel computing, not only because each inversion problem in the first identification phase is independent of the others, but also because each approximation for the gradient of the objective functional (i.e., each index j in Eq. (3.2)) can be solved independently. As such, the increasing number of the shape parameters and initial estimates can be counteracted by a proportional increase in the number of processors dedicated to these computations.

3.4 A divide-alternate-and-conquer strategy for detecting multiple scatters

For a single arbitrarily shaped scatterer a gradient-based minimization method that was enhanced with a two-phase divide-and-conquer methodology was described earlier. In the first phase, the objective is to deterring the approximate location of a target scatterer by using a minimal number of unknown shape parameters, so that multiple initial estimates with simple geometries (e.g., straight lines for a curved crack, or circles for an arbitrarily shaped void or inclusion) are uniformly distributed over the entire spatial domain, and then the values of objective functional of all estimated sets at the converged locations are investigated by carrying out independent identification of each set.

From the resultant data sets, the global minimizer can be easily distinguished

from local minimizers by comparison of the objective functional values, because the value the global minimizer yields, should be lower than those of the local minimizers. At the second phase, the simple geometry of the approximately localized estimate is iteratively refined using parametric cubic splines. In order to enhance the reconstruction of the estimated scatterer's shape, new control points are inserted between existing ones until either a pre-determined error norm is attained or the total number of control points exceeds a pre-determined number.

Here, the two-phase divide-and-conquer strategy is modified to identify multiple scatterers with arbitrary shapes. That is, we hold on to the divide-and-conquer approach in the first step to seek and localize multiple global minimizers, and an alternate-and-conquer approach is subsequently employed to delineate the boundary of each scatterer using cubic splines. The applicability of these approaches to the case of multiple scatterers will be discussed and demonstrated in detail later in Chapter 4, with the assistance of numerical experiments.

CHAPTER 4

Numerical Experiments

Herein, the forward dynamic XFEM solver is rigorously verified first using several benchmark solutions. This is followed by a set of simulated tests through which the proposed shape localization and identification method is observed to work remarkably well. A study on how the deployment configuration of the sensors affects the solution multiplicity of the inverse problem is also provided.

4.1 Verification of the dynamic XFEM implementation

Forward benchmark problems for a line crack, a void, and an interfacial crack are solved in order to verify our implementation of dynamic XFEM. The XFEM solutions are compared either with analytical solutions, when possible, or solutions obtained using conventional FEM.

4.1.1 Stationary mode-I semi-infinite crack problem

We obtain the XFEM solution for the setting seen in Figure 4.1(b), where we consider a mode-I crack within a plane-strain (infinite extent in the anti-plane direction) two-dimensional solid specimen subjected to a uniform tensile stress, $\sigma(t) = \sigma_0 H(t)$, where $H(t)$ denotes the unit step function, given by

$$H(t) = \begin{cases} 0 & \text{if } t < 0, \\ 1 & \text{if } t \geq 0. \end{cases} \tag{4.1}$$

The domain length is $L = 10$ m; the crack length is $a = 5$ m; and the vertical

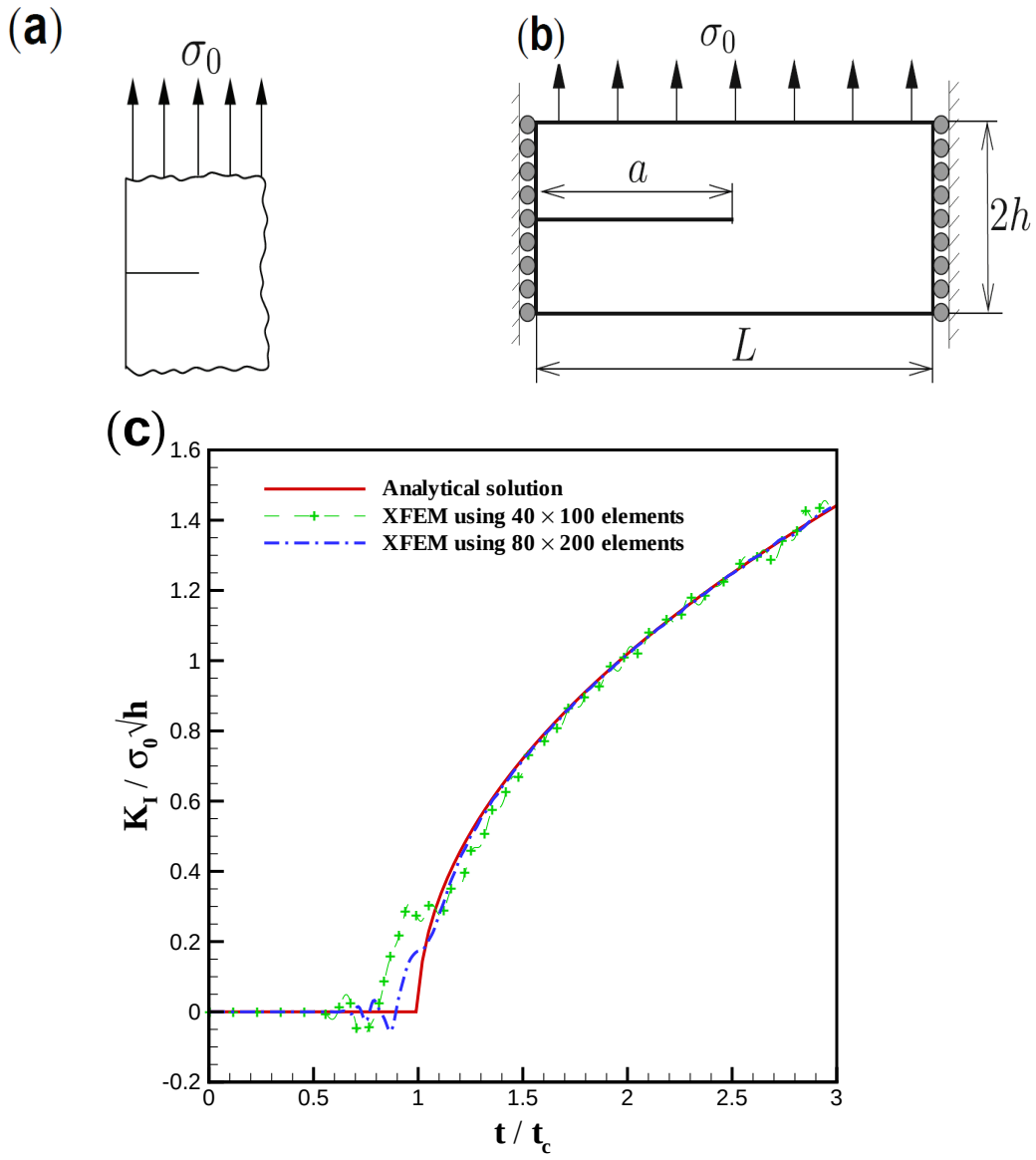

Figure 4.1: (a) An infinite plate with a crack under a plane-strain setting, for which an analytical solution is available; (b) A stationary crack within a bounded plane-strain two-dimensional solid domain model, which is used for obtaining the XFEM solution that corresponds to the analytical solution of the setting (a); (c) The normalized stress intensity factor as a function of normalized time for 40×100 and 80×200 element meshes.

position of the crack from the top surface is $h = 2$ m. Two regular meshes—namely, 40×100 and 80×200—are used, which comprise four-noded quadrilateral elements. The material is linear elastic, having the parameters given in Table 4.1.

Table 4.1: Material constants for the mode-I semi-infinite specimen.

Material constant	Value
Young's Modulus, E	200 GPa
Poisson's ratio, ν	0.3
mass density, ρ	8000 kg $\cdot$ m^3
tensile stress, σ_0	500 MPa

The analytical solution for the mode-I stress intensity factor, K_I, was given by Freund (1990) for the case of a infinite plate with a crack, as seen in Figure 4.1(a). While the XFEM solution for the bounded two-dimensional solid domain model (shown in Figure 4.1(b)) contains a rigid body mode, this ill-posed boundary condition is needed to render the stress solution identical to the problem in Figure 4.1(a). Nevertheless, it is valid to compare the analytical solution with this XFEM solution only until the reflected stress wave field of the XFEM solution from the bottom boundary reaches the crack-tip. Therefore, the total XFEM simulation is limited, in this particular problem, to $t \leq 3t_c := 3h/c_d = 1.009 \times 10^{-3}$ sec, where c_d is the dilatational wave speed. Since the tensile wave reaches the crack at time t_c, the analytical mode-I stress intensity factor can be written as,

$$K_I = \begin{cases} 0 & \text{if } t < t_c, \\ \dfrac{2\sigma_0}{1-\nu}\sqrt{\dfrac{c_d(t-t_c)(1-2\nu)}{\pi}} & \text{if } t \geq t_c. \end{cases} \tag{4.2}$$

Figure 4.1(c) displays the normalized stress intensity factor as a function of normalized time for the coarse mesh (40×100) and the finer mesh (80×200), where it can be seen that the XFEM results show a very good agreement with the analytical solution. Inevitably, some error near $t = t_c$ occurs, because XFEM

Table 4.2: K_I/K_0 and K_{II}/K_0 for centre-crack under remote tension.

	Analytical solution	Present XFEM	Sukumar et al. (2004)
K_I/K_0	1.008	1.010	1.010
K_{II}/K_0	-0.1097	-0.1049	-0.1126

begins to calculate K_I from the vicinity of the crack-tip region before the tensile stress wave reaches the crack-tip. The finer mesh yields better results near $t = t_c$, because a smaller region retains the same number of elements (Menouillard et al., 2010).

4.1.2 Elastodynamic Mode I center-crack problem

A rectangular bar with a centrally located crack shown in Fig. 4.2 is loaded in the axial direction by uniform tension $P = \sigma_0$. The material of the strip is linear elastic, having Young's modulus $E = 200$ GPa, Poisson's ratio $\nu = 0.3$, and density $\rho = 5000\,\mathrm{kg/\,m^3}$. The normalized mode I stress intensity factor $K_I/\sigma_o\sqrt{\pi a}$ is plotted against time t, also in Fig. 4.2. The numerical results determined by Dynamic XFEM are in very good agreement with Chen's results (1975).

4.1.3 A void in an aluminum medium

An aluminum host with a void is considered. The excitation is applied on the upper boundary, while all of the other boundaries are fixed. The dynamic XFEM results are compared to those obtained from the conventional FEM solver. Figure 4.3 displays snapshots of the amplitudes of displacement fields at 14 μs, 20 μs, and 26 μs, obtained via dynamic XFEM and conventional FEM. Excellent agreement is observed between the two solutions.

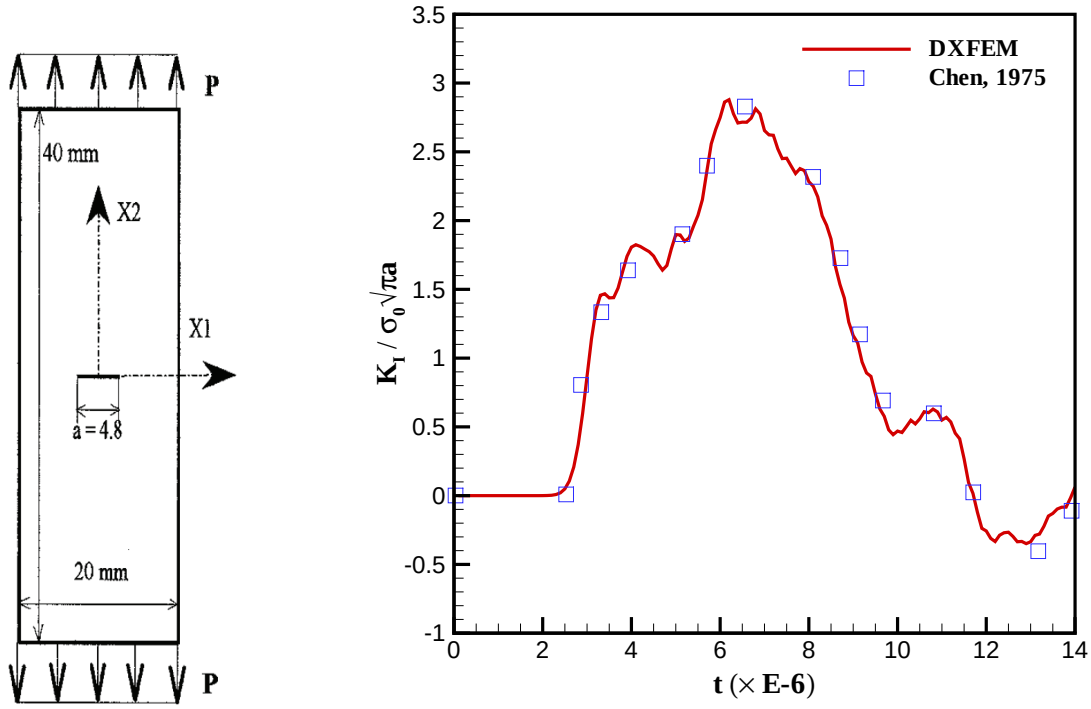

Figure 4.2: Rectangular bar with a centrally located crack: problem geometry and boundary conditions (left); normalized K_I computed via XFEM compared with Chen's (1975) solution (right).

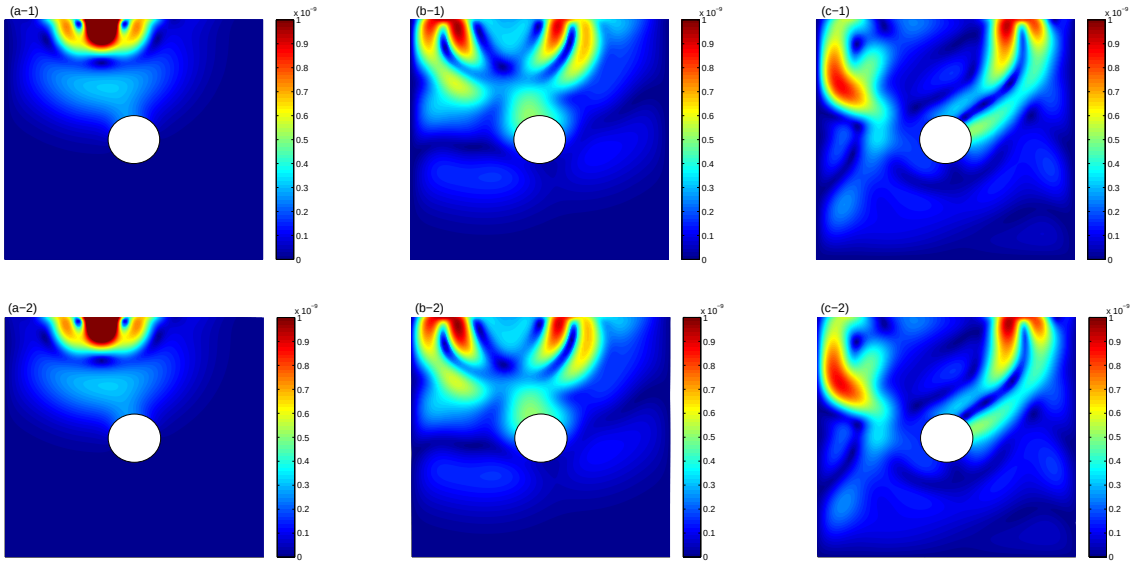

Figure 4.3: The amplitudes of the displacement field of elastic waves in the isotropic homogeneous medium (aluminum) with a void at (a) 14 μs, (b) 20 μs, and (c) 26 μs. (a-1, b-1, c-1): XFEM results; (a-2, b-2, c-2): conventional FEM results.

4.1.4 A crack in infinite bi-material media

A bi-material interface crack problem is considered. The crack is located along the interface of two elastic homogeneous isotropic materials under Mode-I loading. A symmetric and semi-infinite half specimen with domain size 20×40, discretized using a 100×200 elements, is considered under plane-strain conditions, as shown in Figure 4.4. The analytical solutions for K_I and K_{II} are given by Rice and Sih (1965), as

$$K_I + \mathrm{i}K_{II} = (\sigma_0 + \mathrm{i}\tau)(1 + 2\mathrm{i}\epsilon)\sqrt{\pi a}(2a)^{-\mathrm{i}\epsilon}, \tag{4.3}$$

where τ is the shear stress; ϵ is the bi-material constant (see Eq. (2.38)); and $2a$ is the crack length. The material constants used for the numerical simulation are chosen as $E_1/E_2 = 22$, $\nu_1 = 0.2571$ and $\nu_2 = 0.3$. In this case, the normalized

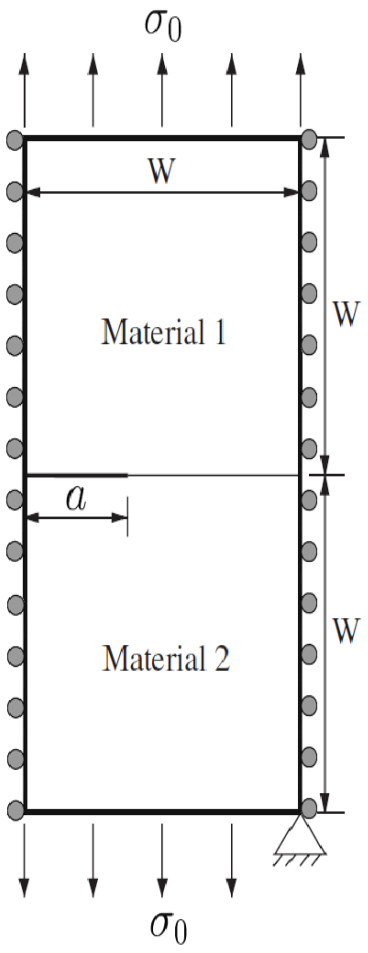

Figure 4.4: bi-material interface crack under remote tension (half-model).

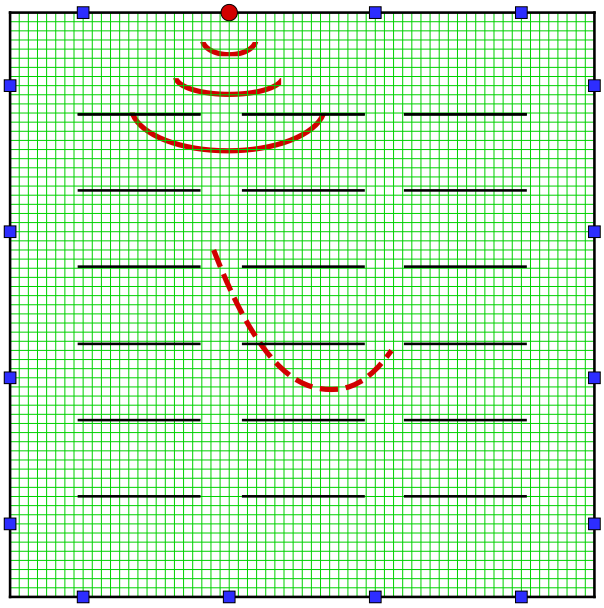

Figure 4.5: A schematic of multiple initial estimates (solid lines) for detecting a single target curved crack (a red dashed line) in two-dimensional bounded specimen of size $0.1\text{m} \times 0.1\text{m}$ with uniform 64×64 mesh; a wave source (a red circle); and sensors (blue squares).

analytical solutions from Eq. (4.3) is

$$\frac{K_I}{K_0} = 1.008, \quad \frac{K_{II}}{K_0} = -0.1097, \tag{4.4}$$

where $K_0 = \sigma_0\sqrt{\pi a}$ and $a = 1$. It may be observed from Table 4.2 that the stress intensity factors are in good agreement with the analytical solutions, and the values obtained from the present XFEM are reasonable, as compared to those of Sukumar et al. (2004).

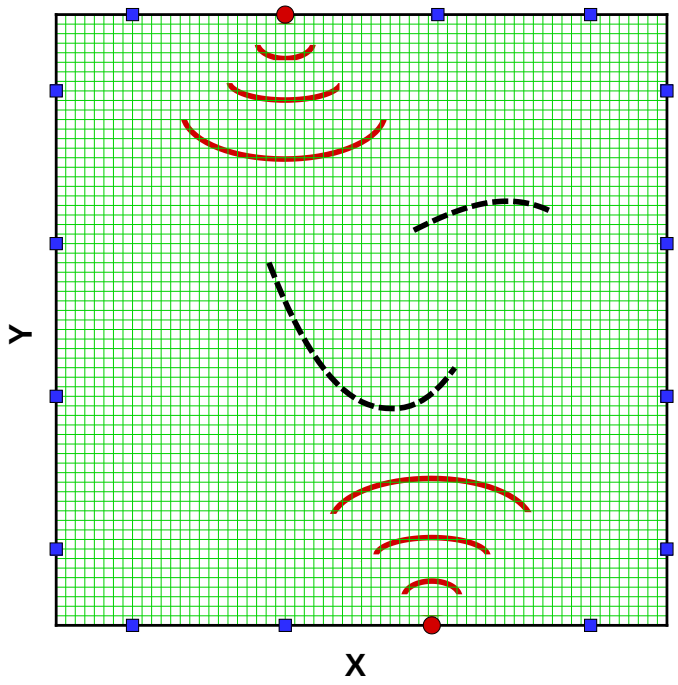

Figure 4.6: A schematic of the experimental setup for numerical implementations of multiple target scatterers (dashed lines): the two-dimensional 0.1m $\times$ 0.1m aluminum specimen surrounded by wave sources (red circles) and sensors (blue squares) is modeled by uniform 64×64 meshes.

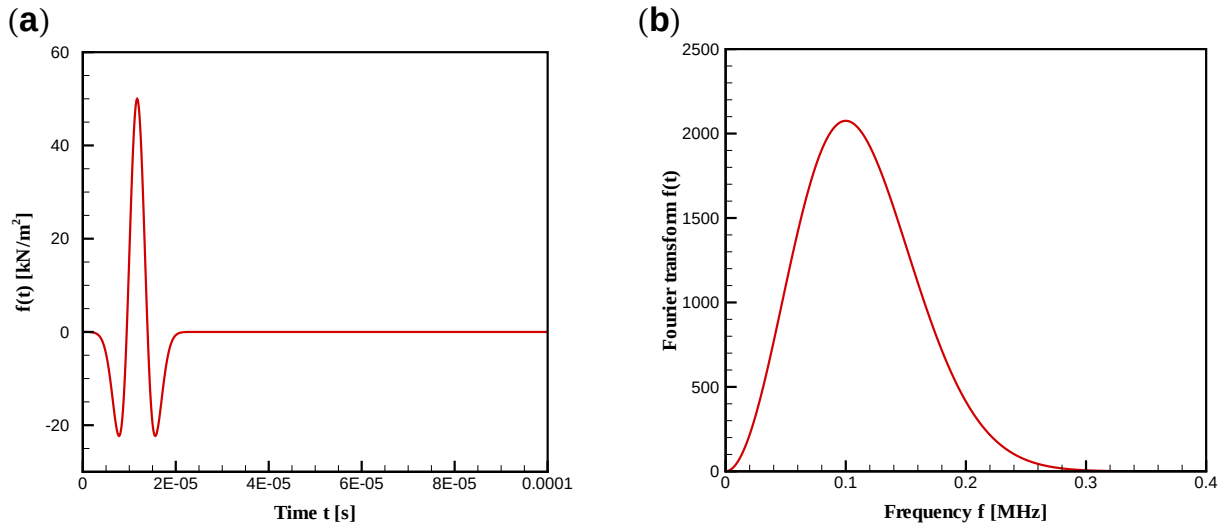

Figure 4.7: The Ricker-pulse loading signal with a central frequency of $f_c = \omega_r/(2\pi) = 0.1$ MHz: (a) the Ricker pulse time signal; (b) Fourier amplitude spectrum of the Ricker pulse signal.

4.2 Description of the problem geometry and boundary conditions

To carry out numerical experiments for multiple arbitrarily shaped cracks, voids, or inclusions (steel), two-dimensional plane-strain homogeneous (aluminum) or heterogeneous (aluminum and steel) specimens are considered. All of these specimens have the same dimensions (i.e., $0.1\text{m} \times 0.1\text{m}$) and are modeled using 64×64 finite element meshes, as shown in Figures 4.5 and 4.6. Either one or two time-dependent loading sources are positioned on the top and bottom surfaces, and multiple sensors are deployed along the boundary of the specimen for detecting a single or multiple target scatter, respectively. The lower left/right corner is assumed to be fixed. The material properties of aluminum and steel are given in Table 4.3.

A modified Ricker pulse with a central frequency $f_c = 0.1$ MHz, whose fre-

quency range is about 0 to $3f_c$ MHz, is used as the excitation signal of each source as shown in Figure 4.7 and is given by:

$$f(t) = \begin{cases} -50 \times \dfrac{(0.25\eta^2 - 0.5)e^{-0.25\eta^2} - 13e^{-13.5}}{0.5 + 13e^{-13.5}} \ \ [\mathrm{kN/m^2}] & t \leq \bar{t}, \\ 0 & t > \bar{t}. \end{cases} \tag{4.5}$$

where $\eta = \omega_r t - 3\sqrt{6}$; $\bar{t} = 6\sqrt{6}/\omega_r$; $\omega_r = 2\pi f_c$; the total time period of observation for each forward simulation is 80 μs; and each time step is 0.1 μs.

It is noted that the finite element mesh size should be smaller than the shortest wavelength calculated using the material property of the host medium and the frequency range of the given excitation source. Also, it is expedient to note that the mesh size and source frequency has an effect on the size of detectable target scatterers. Specifically, scatterers that are smaller than a single element—or scatterers smaller than the smallest wavelength that can be propagated by the forward solver—can not be detected/localized, in general.

Table 4.3: Material properties of aluminum and steel. Young's modulus, E; Poisson's ratio, ν; mass density, ρ.

Material	Property	Value
Aluminum	E	71.5 GPa
	ν	0.33
	ρ	2800 kg/m^3
Steel	E	200 GPa
	ν	0.25
	ρ	7800 kg/m^3

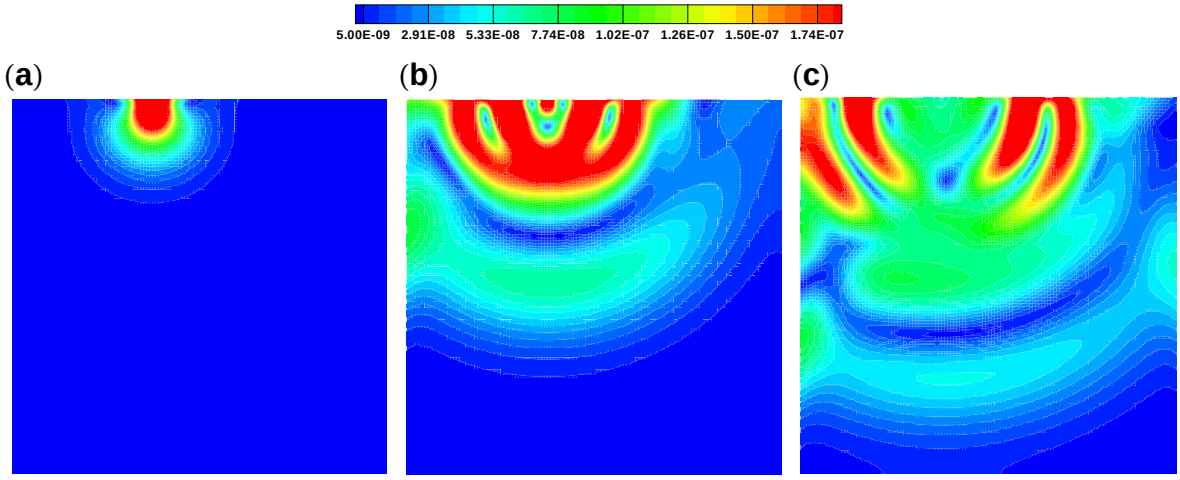

Figure 4.8: The amplitudes of the displacement field of elastic waves within the isotropic homogeneous medium (aluminum) at (a) 9 μs, (b) 17 μs, and (c) 21 μs.

4.3 Simulated inverse-scattering tests for various multi-sensor deployment patterns

Figure 4.8 displays the snapshots of the spatial distribution of wave responses of the two-dimensional aluminum specimen without any embedded scatterers. The compressional and shear waves are clearly observed. The distribution of the magnitude of the objective functional with respect to two shape parameters x_c and y_c—i.e., the x and y coordinates of the centroid of a horizontal line crack whose length is 0.025m—are shown in Figure 4.9. That is, we compute the value of the objective functional for a given (estimated) line crack (e.g., the blue dotted line in Figure 4.9(a-1)) as its centroid is varied through the entire domain for each case of 1, 3 or 15 sensors (shown in Figures 4.9(a), (b), (c), respectively). As it may be observed from Figure 4.9, for every sensor deployment case, the objective functional has a global minimum. As one might expect, the attraction basins become larger and the objective functional becomes less wrinkled (i.e., fewer local minima) with increased number of sensors.

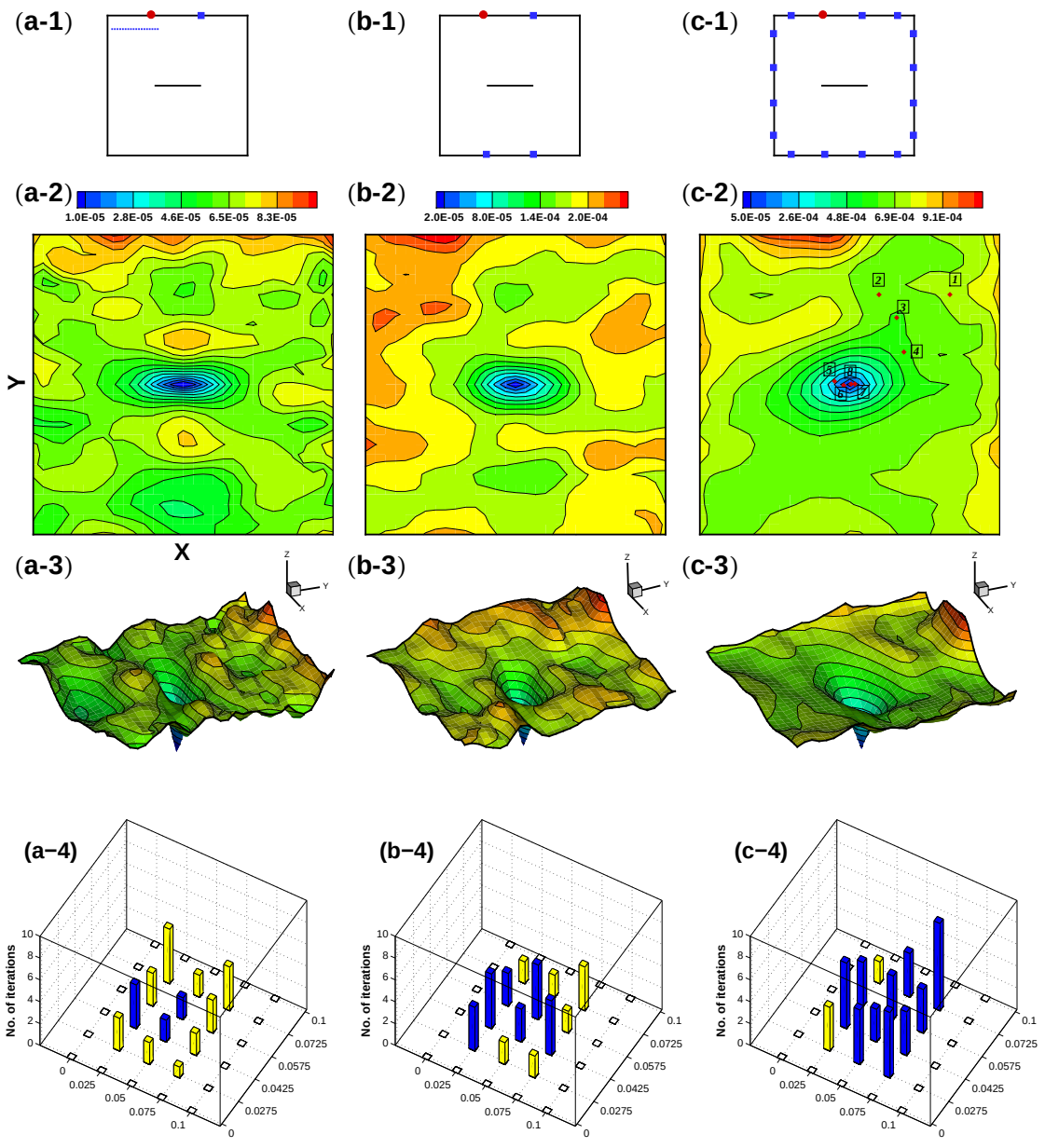

Figure 4.9: Two- and three-dimensional contour plots of the objective functional for (a) 1, (b) 3 and (c) 15 sensors deployed for a fixed-length (2.5 cm) crack that is relocated throughout the host domain. The solid lines indicate the actual cracks; the blue dotted line in (a-1) is one of initial estimates. The last row displays histograms of the number of iterations for 12 initial estimates distributed evenly on the host domain. The blue and yellow bars indicate sequences that converged to the global minimizer (i.e., the actual crack location) or some local minimum, respectively.

Figure 4.9(c-2) also provides a visualization of the tracking process for finding the global minimum using the gradient-based optimization. It starts at an arbitrary initial guess location marked as 1 and then, converges at 8, corresponding to the identified location parameters $x_c = 0.05031,\ y_c = 0.05013$, which are very close to the target location—i.e., center of the line crack at $x_c = 0.05,\ y_c = 0.05$.

Figures 4.9(a-4, b-4, c-4) display the histograms that indicate the number of iterations corresponding to 12 different initial estimates that were evenly distributed on the host domain for each of the three different sensor configurations. The blue and yellow bars on these histograms indicate results that converged to the global minimizer (i.e., the actual target location) and to local minima, respectively. The height of each bar indicates how many iterations took place during each trial. The iterations were terminated when $|\mathcal{L}_{(n)}| \leq 3 \times 10^{-5}$ or when $\left|\mathcal{L}_{(n-1)} - \mathcal{L}_{(n)}\right| < 10^{-6}$ (for slowly converging iterations). It is useful to note here that during these numerical experiments, the former criterion was satisfied *only* when the iterations converged to the global minimizer, whereas the latter criterion was *always* the cause of termination when the iterations wandered, or they were stuck at a local minimum.

An interesting observation can be made regarding the convergence behavior for different sensor configurations: It took fewer iterations for the optimizer to find the solution when the number of sensor were fewer. However, for fewer sensors, only a small subset of initial guesses were successful. As the number of sensors were increased, almost all of the initial guesses converged to the actual solution; but it took more iterations to satisfy a given absolute convergence criterion (i.e., $|\mathcal{L}_{(n)}| \leq 3 \times 10^{-5}$). While this may appear somewhat counter-intiutive, it is actually observable in Figures 4.9(a-1, b-1, c-1) wherein it can be clearly seen that the objective function values are, in fact, increasing throughout the feasible domain, as the number of sensors are increased (while at the same time the global minimizer becomes nearly the only basin of attraction). As such, it is more difficult to

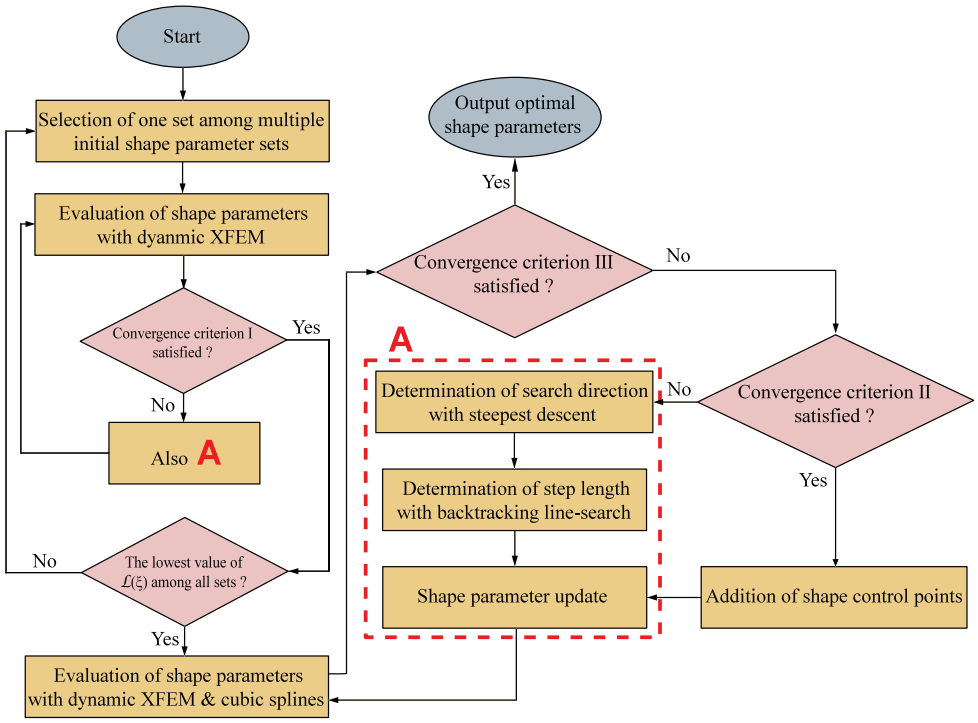

Figure 4.10: A flowchart for identification of a single arbitrarily-shaped scatterer.

satisfy the absolute convergence criterion when there are more data to assimilate. This, however, is essentially a scaling problem, and it appears that the simple remedy is to normalize the objective function by the number of sensors.

4.4 Identification of several types of single and multiple scatterers in homogeneous and bi-material host media

4.4.1 Identification of an arbitrarily shaped single scatter using the divide-and-conquer strategy

We now investigate the performance of the proposed identification method for three different types of internal scatterers—a crack, a void, and an inclusion—with arbitrary shapes in a homogeneous and a bi-material host.

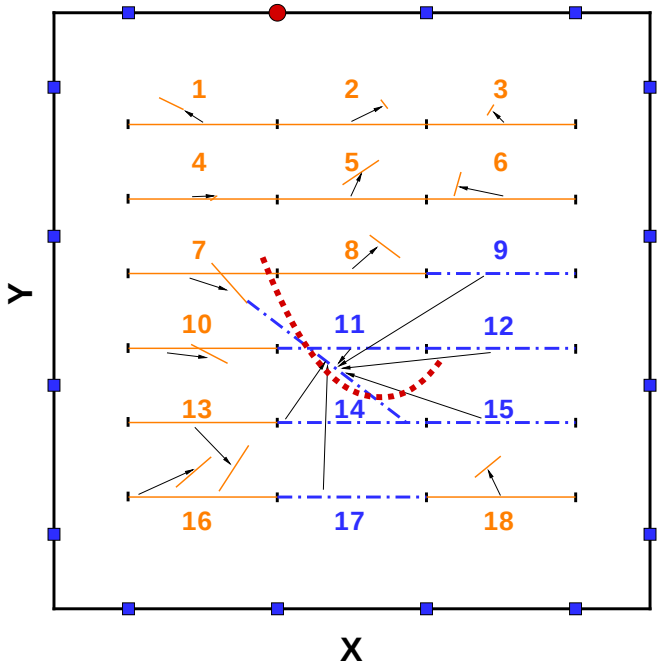

Figure 4.11: The demonstration of the step of the divide-and-conquer approach: eighteen initial (straight line crack) estimates are used to search for a curved crack (the red dashed line): the initial estimated (blue dashed-dotted lines marked with numbers 9, 11, 12, 14, 15 and 17) converged near the global minimum; the others (orange solid lines) fell either into local minima or did not converge at all.

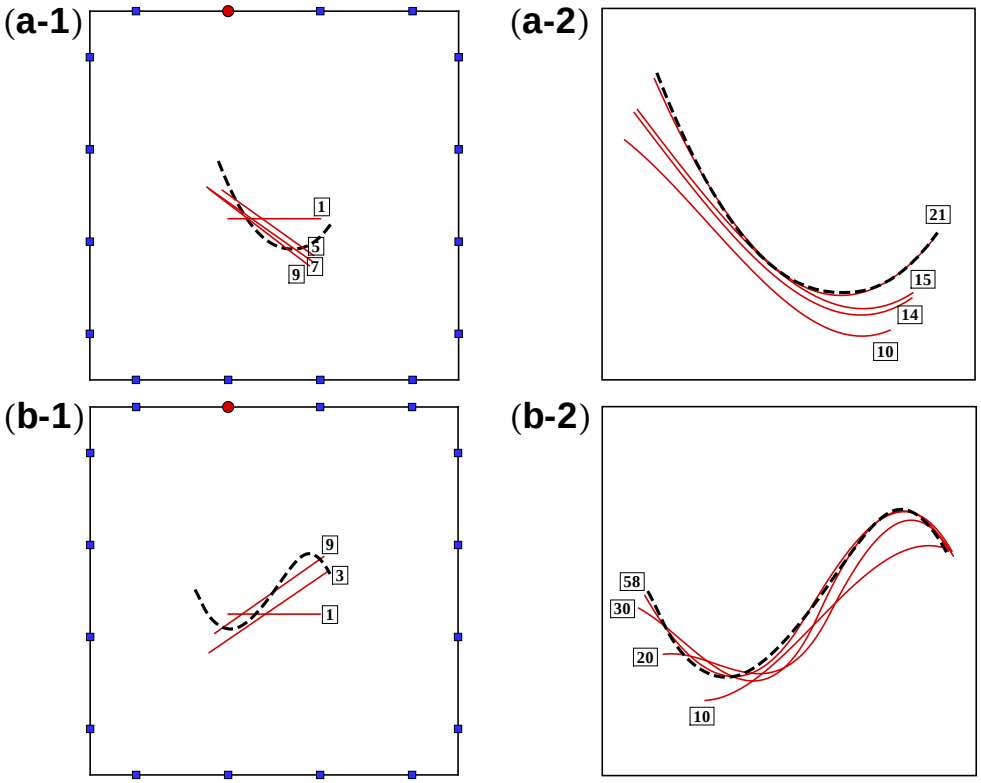

Figure 4.12: Evolutionary detection process for (a) L-shaped and (b) S-shaped curved cracks (dashed line) using first (a-1, b-1) a straight line, and subsequently (a-2, b-2) cubic splines. The iteration number is shown with a boxed numeral (initially estimated scatterer is marked as 1).

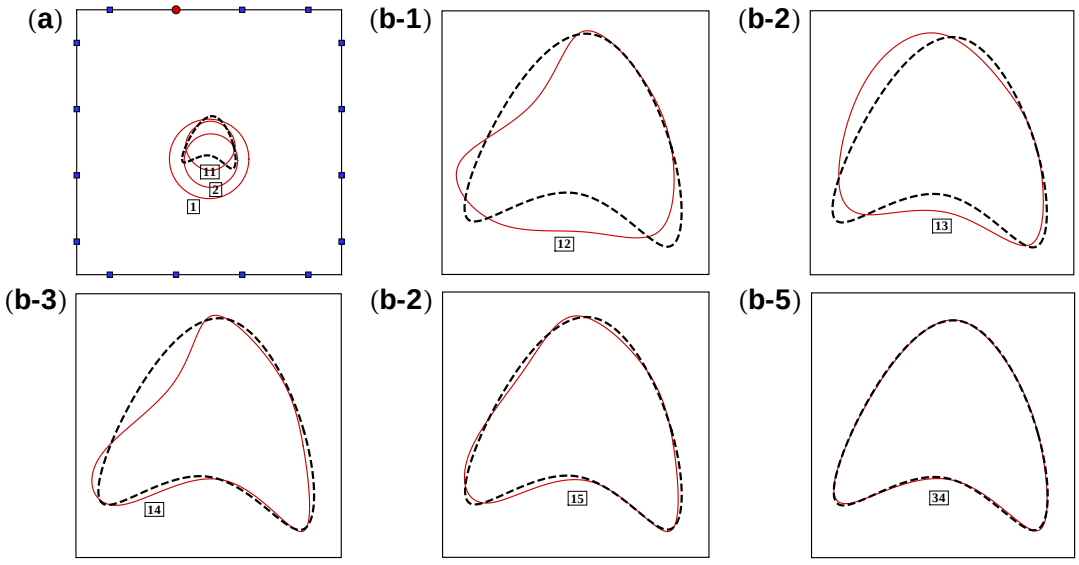

Figure 4.13: Evolutionary detection process for a concave-shaped void (dashed line) using first (a) a circular shape, and subsequently (b) parametric cubic splines. The iteration number is shown with a boxed numeral (initially estimated scatterer is marked as 1).

The shape-parameter identification process described briefly earlier comprises two main steps/phases. As illustrated in Figure 4.10, first, multiple initial estimates are seeded and ultimately one solution—corresponding to the lowest converged value of the objective functional—among the entire set of multiple initial scatterers is selected. This *first step* corresponds to the flowchart region from "Start" to the second diamond-shaped "decision box" (i.e., the diamond that includes the convergence criterion C_I) in Figure 4.10. In the second phase, the geometric representation of the scatterer is switched to a set of cubic splines and a second round of optimization is carried out. This corresponds to the remainder of the flowchart—i.e., the region from the second decision diamond to the

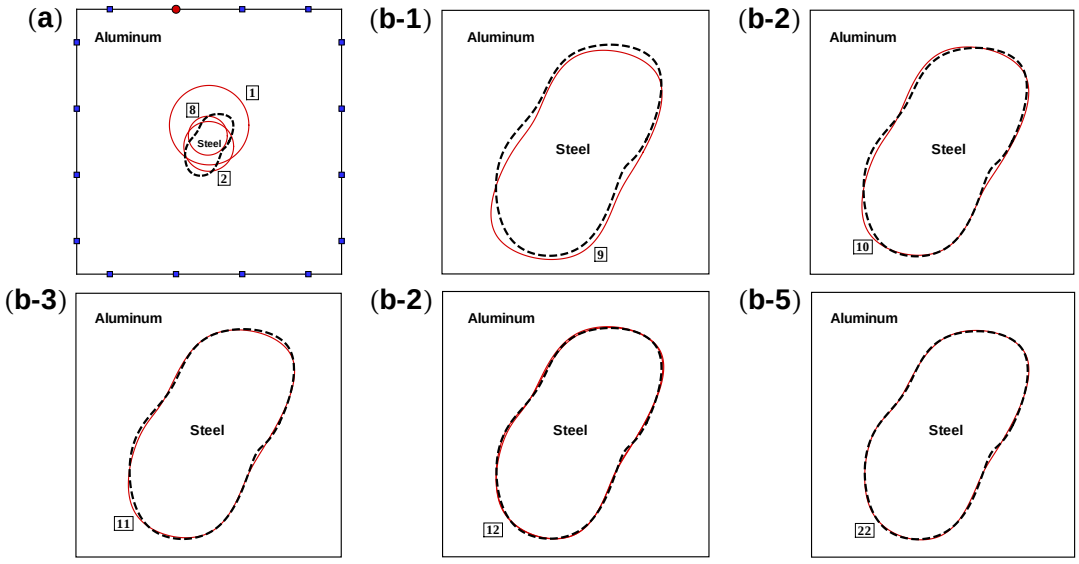

Figure 4.14: Evolutionary detection process for a potato-shaped inclusion (dashed line) using first (a) a circular shape, and subsequently (b) parametric cubic splines. The iteration number is shown with a boxed numeral (initially estimated scatterer is marked as 1).

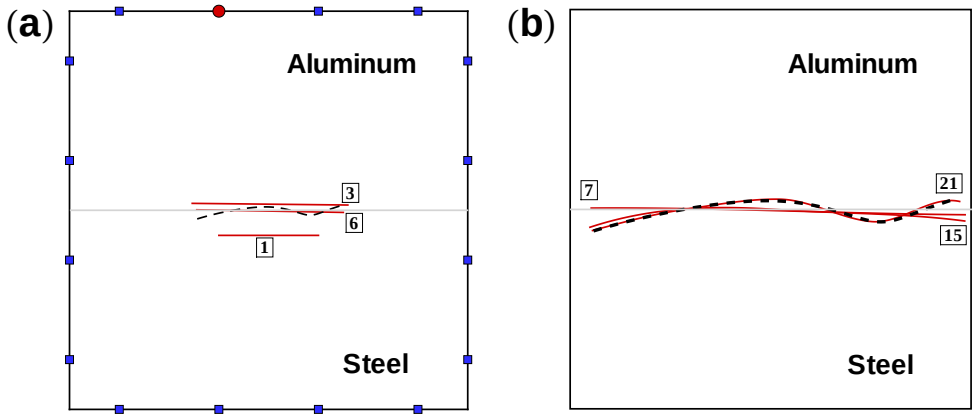

Figure 4.15: Evolutionary detection process for a curved crack (dashed line) in bi-material (aluminum (upper-half plane) and steel (lower-half plane)) using first (a) a straight line, and subsequently (b) parametric cubic splines. The iteration number is shown with a boxed numeral (initially estimated scatterer is marked as 1).

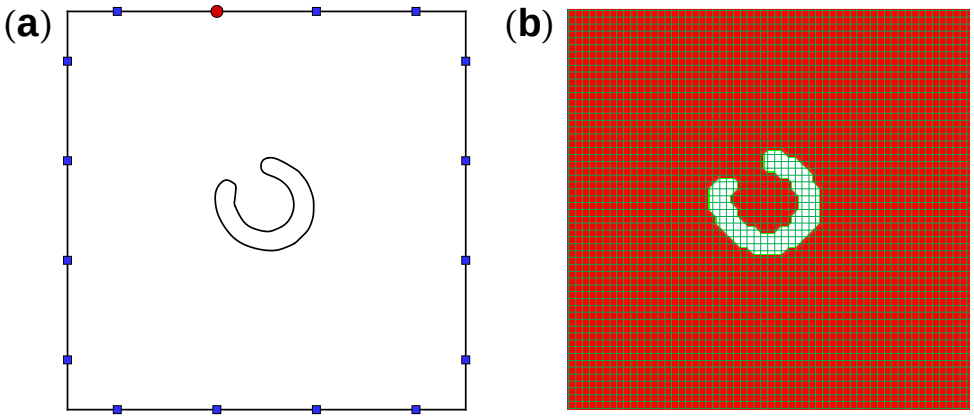

Figure 4.16: (a) A horseshoe-shaped scatterer; (b) the contour plot for the horseshoe-shaped scatterer with the value 1 outside the scatterer (red) and -1 inside the scatterer (white).

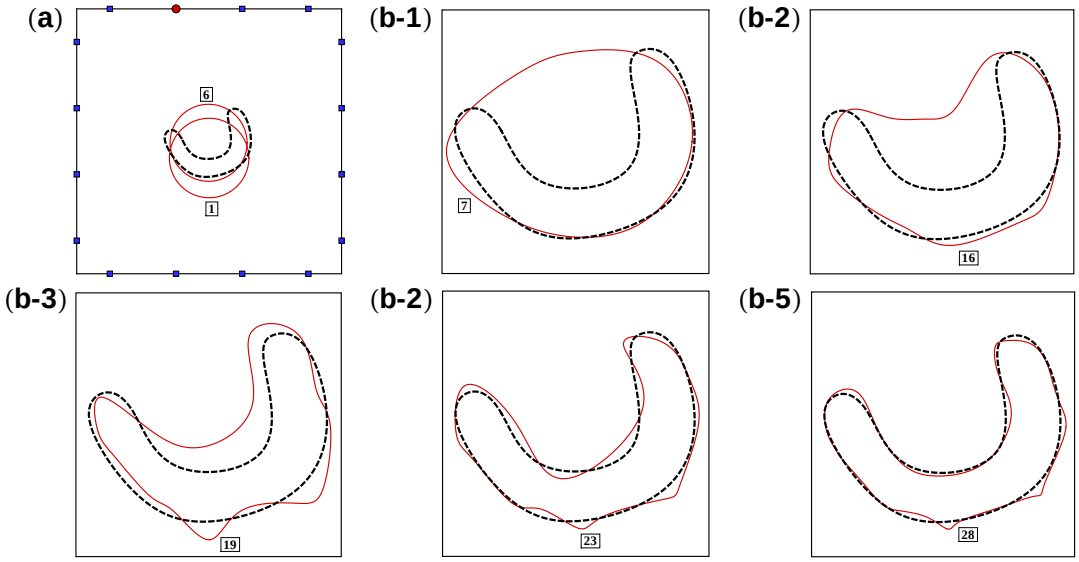

Figure 4.17: Evolutionary detection process for a horseshoe-shaped void (dashed line) using first (a) a circular shape, and subsequently (b) parametric cubic splines. The iteration number is shown with a boxed numeral (initially estimated scatterer is marked as 1).

convergence criteria II and III in Figure 4.10. These criteria are chosen as

$$C_{I(n)}\left(=C_{II(n)}\right)=\frac{\left|\mathcal{L}_{(n-1)}-\mathcal{L}_{(n)}\right|}{\mathcal{L}_{(n)}}\ \leq\ 10^{-3},$$
$$C_{III(n)}=\mathcal{L}_{(n)}\ \leq\ 1.1\times10^{-6}\quad\text{or}\quad\mathcal{P}_{(n)}>16, \tag{4.6}$$

where $\mathcal{P}_{(n)}$ indicates the total number of shape control points at the current step; and $\mathcal{L}_{(n-1)}$ and $\mathcal{L}_{(n)}$ are the values of the objective functional at two successive iterations. In the present study, the control points are added between each point and re-positioned by the cubic spline method, whenever C_{II} is satisfied. $\mathcal{P}_{(n)}$ is defined through the recursive relationships $\mathcal{P}_{(n)}=2\mathcal{P}_{(n-1)}-1$ with $\mathcal{P}_1=2$ for a curved crack, and $\mathcal{P}_{(n)}=2\mathcal{P}_{(n-1)}$ with $\mathcal{P}_1=4$ for a void/inclusion, respectively.

Figure 4.19 displays the convergence behavior of the uniformly distributed multiple initial estimates in an aluminum specimen based on the divide-and-conquer strategy. Each initial estimate has four shape parameters—*viz.*, the x and y coordinates of their end points. The orange-colored initial scatterers (marked with numbers 1–8, 10, 13, 16 and 18) are relatively far from the target scatterer (the red dashed line), and converged to various local minima (i.e., C_I was satisfied) or wandered until the maximum number of iterations were reached (here 100). On the other had, the initial estimated marked with blue dashed-dotted lines (marked with numbers 9, 11, 12, 14, 15, 17) converged near the scatterer (i.e., to the global minimum of the first phase). From here on, we can choose only one solution out of the converged set {9, 11, 12, 14, 15, 17}, which yielded the lowest value of objective functional and continue on with the second phase.

The performance of the proposed identification method for various types scatterers are demonstrated in Figures 4.12 (two different curved cracks), 4.13 (concave void), 4.14 (potato-shaped inclusion), 4.15 (curved crack at a bi-material interface) and 4.17 (horse-shoe-shaped void). In these figures, the iterative procedure is visualized by displaying the successive (converging) estimates of the scatterer.

For the initial estimates of the first phase the divide-and-conquer approach,

regular geometries that are appropriate for the type of scatterer—namely, a straight line for cracks, and a circular void/inclusion for the rest—are used to scan the approximate position and geometry. Here, the convergence and segmentation of the scatterer is decided based on criteria C_{II} and C_{III} in Equation (4.7), respectively. In all of the aforementioned experiments, reasonable estimates were obtained in fewer than 30 iterations for most cases (only an s-shaped crack required 58 iterations).

Two different curved cracks were considered in Figure 4.12: (a) an L-shaped curved crack and (b) an S-shaped curved crack, wherein each of the target geometries was successfully reconstructed by using two and nine control points, marked as the iteration number 21 and 58, respectively.

Next, a concave-shaped void marked as 34 and a potato-shaped inclusion marked as 22 shown in Figures 4.13 and 4.14 were effectively detected with eight control points.

The converged estimate of the scatterer depicted by nine control points—marked as 21 in Figure 4.15—accurately reconstructed an arbitrarily-shaped curve located between bi-material interfaces, in spite of the disturbance of wave reflection from the bi-material interface.

The proposed identification method was finally applied to detect a fairly complex (a horse-shoe-shaped) scatterer (Fig. 4.16-a) by using the approximate level set function shown in Figure 4.16-b. Unlike the earlier examples shown in Figures 4.13 and 4.14, the centroid of the horseshoe-shaped scatterer is outside the convex-hull of its geometry, which could cause difficulties in both phases of the identification. In the current study, it was approximately described by using a level set function defined as $+1/-1$ at the nodes on the outside/inside of the geometry, based on the cubic spline functions for each segmentation. Figure 4.17 displays the sequence of shape estimates for this problem: the final estimate scatterer comprised sixteen control points, closely matched the target scatterer at

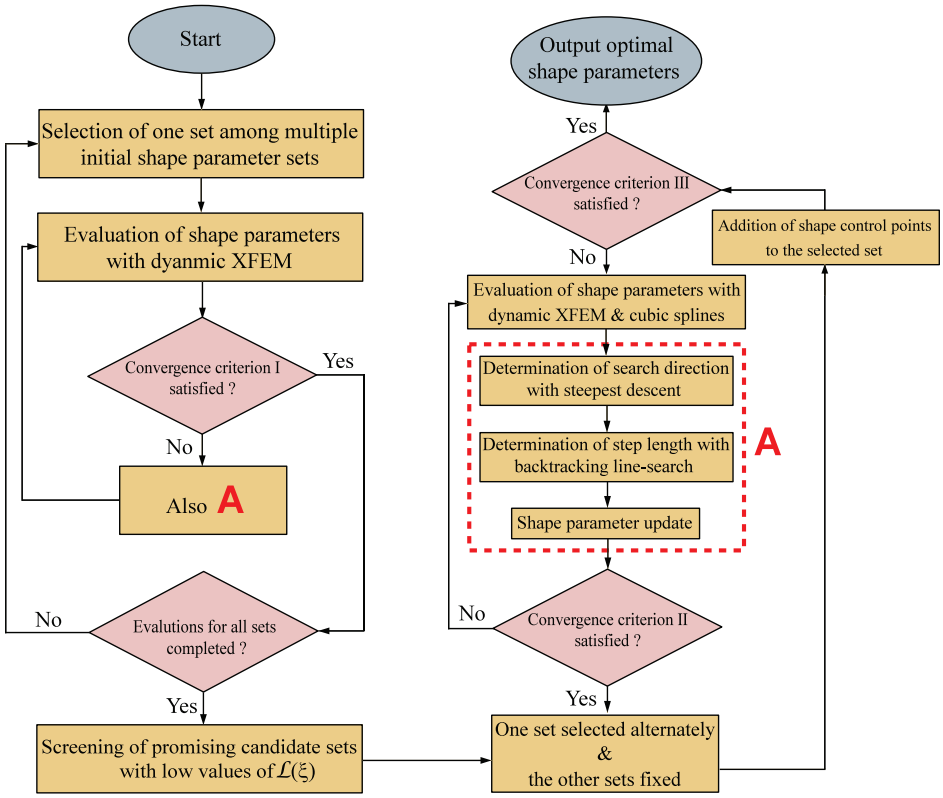

Figure 4.18: A flowchart for identification of multiple arbitrarily shaped scatterers: the left and right column on the flowchart are correspond to the divide-and-conquer and alternate-and-conquer strategies, respectively.

iteration no. [28].

4.4.2 Identification of arbitrarily shaped multiple scatters using the alternate-and-conquer strategy

In this section, a divide-alternate-and-conquer algorithm for localization and shape identification of multiple scatterers is described in detail, and an example is provided. This approach is literally divided into two main—namely, the divide-and-conquer and the alternate-and-conquer—procedures. These respectively correspond to the left and right columns of the flowchart given in Figure 4.18. Here, the convergence criteria I, II, and III corresponding to C_I, C_{II}, and

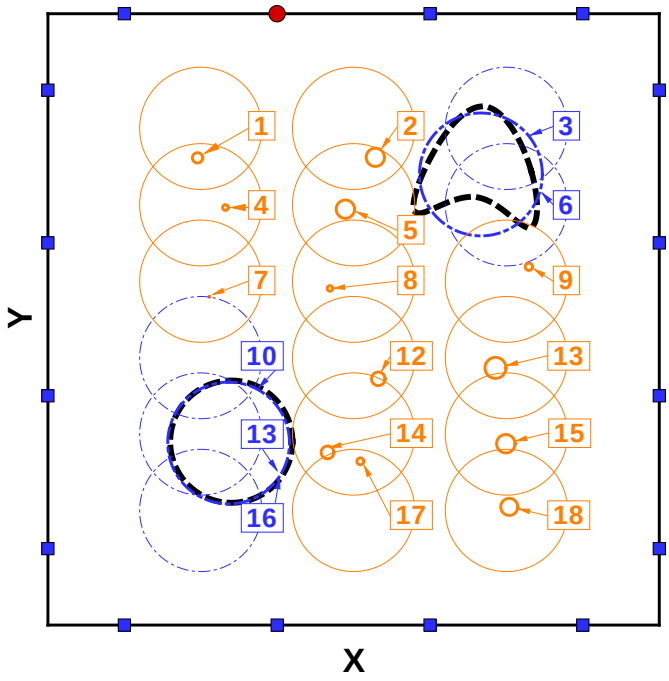

Figure 4.19: An illustrative example of the divide-and-conquer approach: Eighteen uniformly-spaced initial estimates (circles) are employed to seek multiple voids (here a circle and an irregularly shaped void, both of which are marked with black dashed lines): the initial estimates (blue dashed-dotted lines marked with numbers 3, 6, 10, 13 and 16) converged near the global minimum; the others (orange solid lines) fell into local minima. Each arrow ($\rightarrow$) indicates the converged locations.

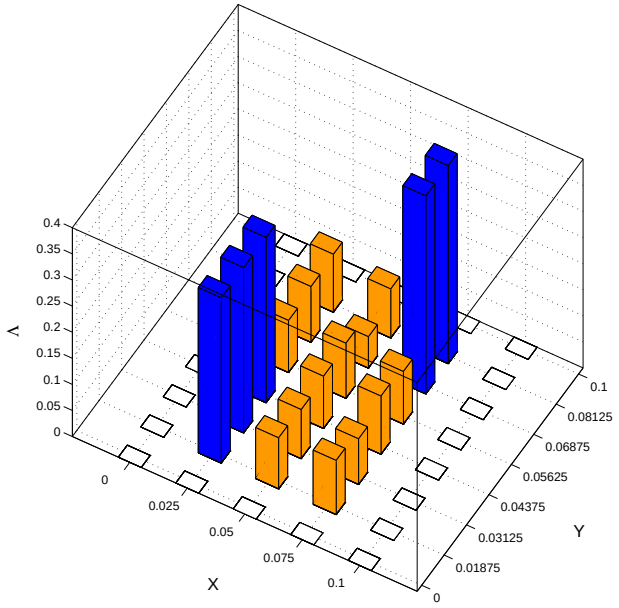

Figure 4.20: Histogram of the normalized objective functional values (Λ_i) for the i-th initial estimates ($i = 1 - 18$). Here, $\Lambda_i = (\langle \mathcal{L} \rangle - \mathcal{L}_i)/\langle \mathcal{L} \rangle$; the bracket $\langle\rangle$ indicates the average value of $\mathcal{L}_{1-18}$.

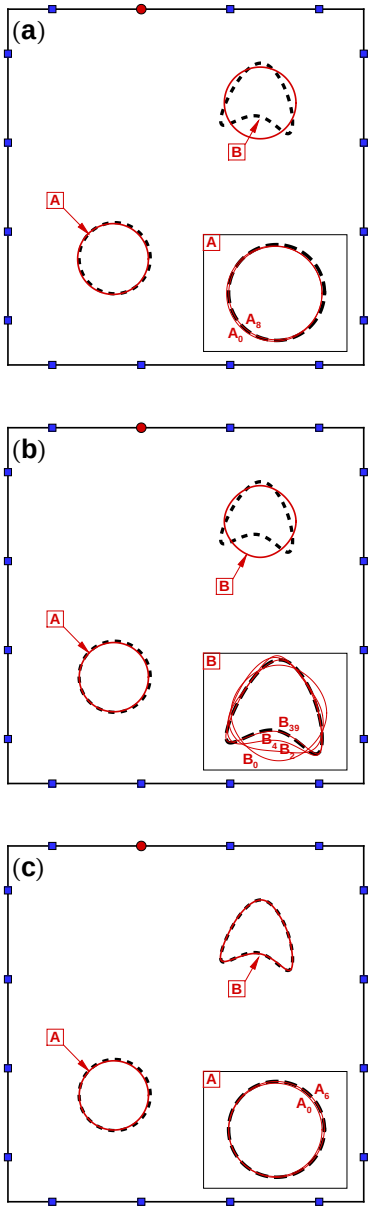

Figure 4.21: A demonstration of the alternate-and-conquer approach: (a) the shape of scatterer A is identified while the scatterer B is held fixed; (b) the shape of scatterer B) is identified while the scatterer A is held fixed; (c) (a)-optimization mode is repeated. Here, the i of A_i/B_i denotes the number of iterations.

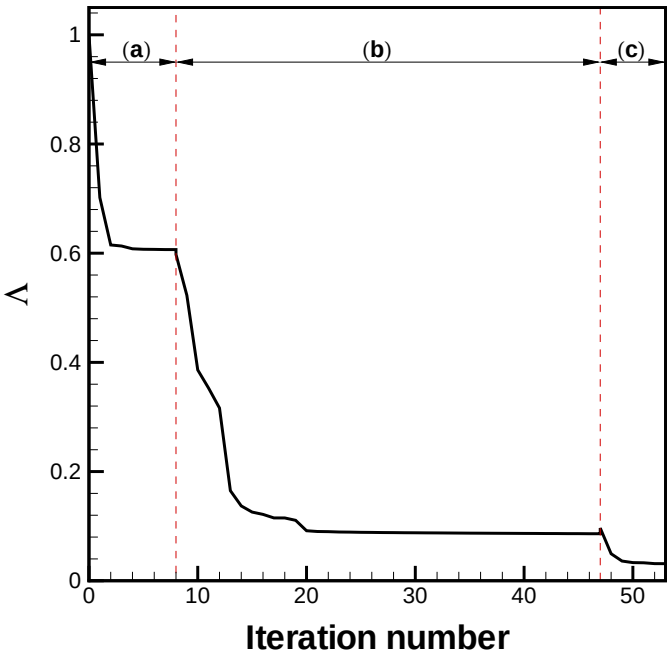

Figure 4.22: The variation of Λ with the iteration number, i, during the detection process (a) to (c) in Figure 4.21 for multiple voids. Here, $\Lambda_i = \mathcal{L}_i/\mathcal{L}_0$.

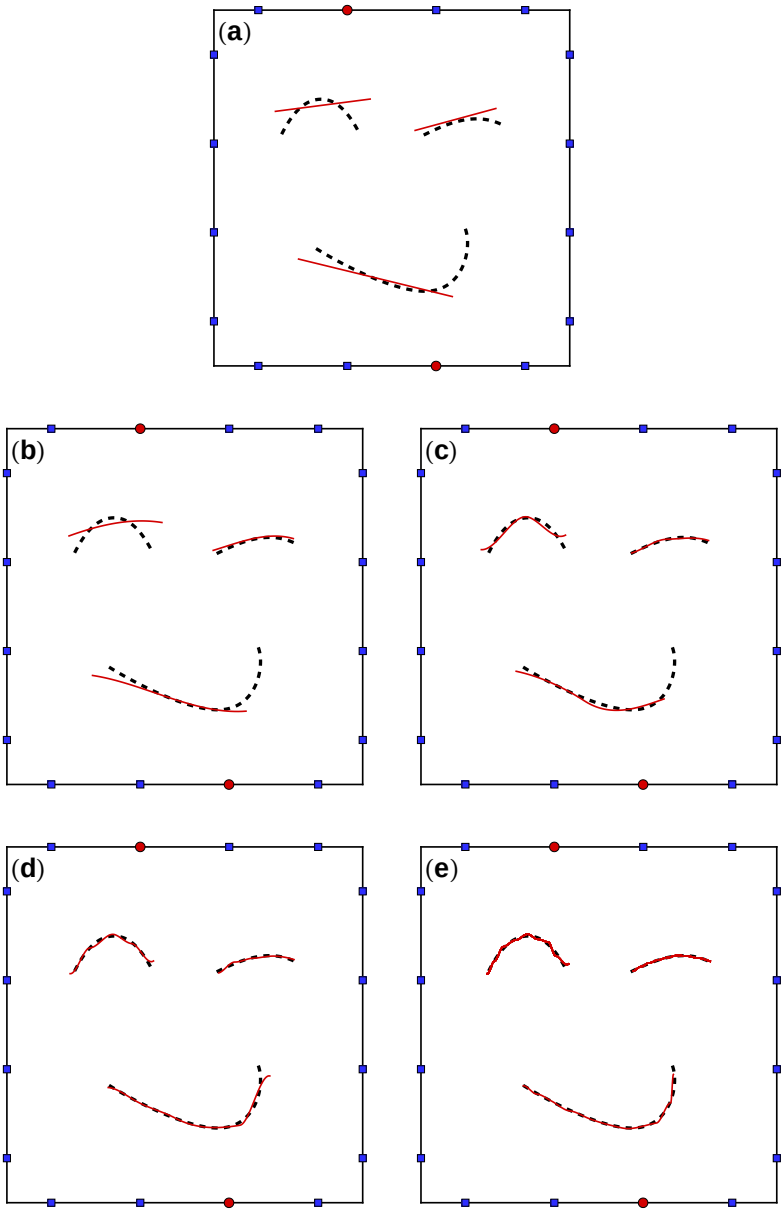

Figure 4.23: Evolutionary identification procedure for multiple curved cracks (dashed lines) from (a) to (e): (a) the estimated scatterers (solid lines) are localized by using the divide-and-conquer strategy; (b)-(e) the scatterers' shapes are refined by using cubic splines and the alternate-and-conquer strategy.

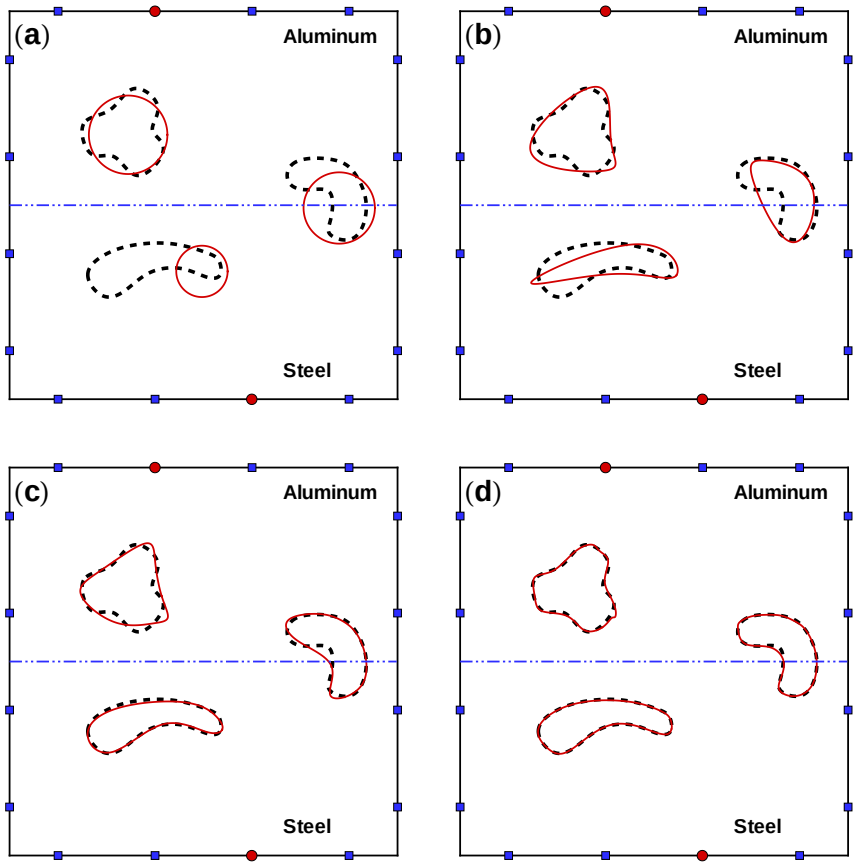

Figure 4.24: Evolutionary identification process for multiple voids (dashed lines) from (a) to (d): (a) the initial-estimated scatterers (solid lines) are localized by using the divide-and-conquer strategy; (b)-(d) the scatterers' shapes are refined by using cubic splines and the alternate-and-conquer strategy.

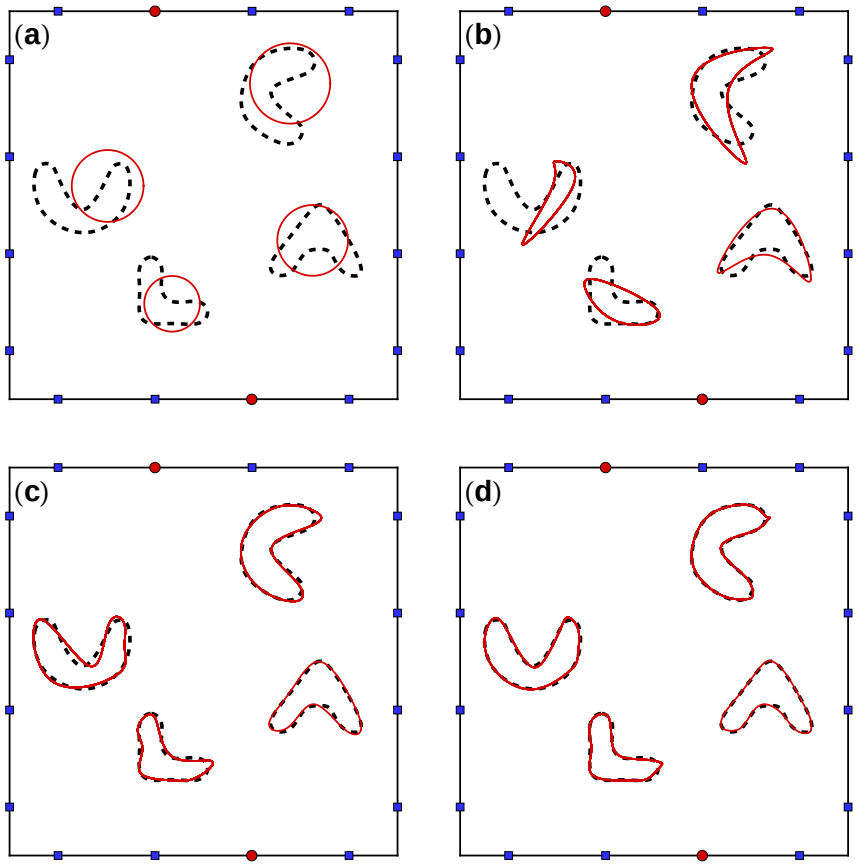

Figure 4.25: Evolutionary identification process for multiple inclusions (dashed lines) from (a) to (d): (a) the initial-estimated scatterers (solid lines) are localized by using the divide-and-conquer strategy; (b)-(d) the scatterers' shapes are refined by using cubic splines and the alternate-and-conquer strategy.

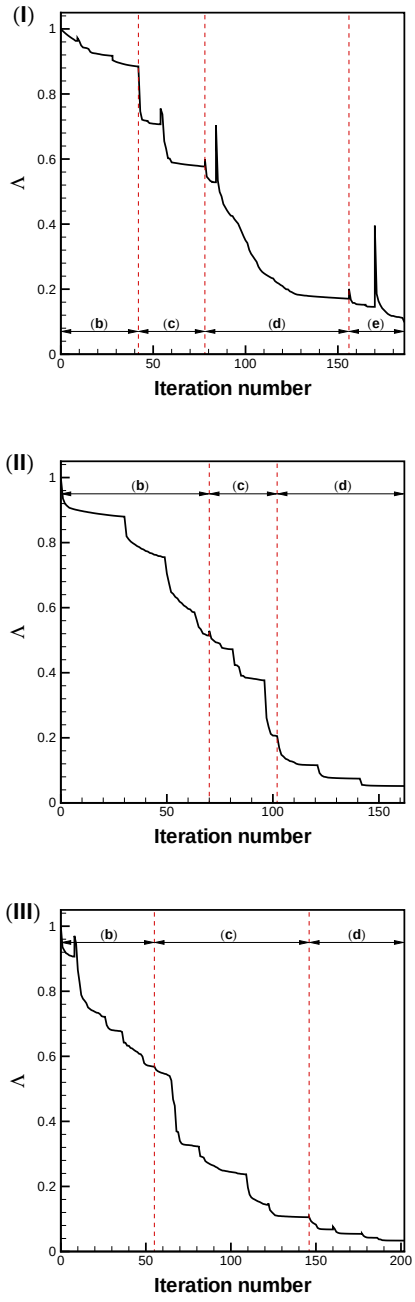

Figure 4.26: The variation of Λ with the iteration number, i, during the alternate-and-conquer process: (I) (b)-(e) in Figure 4.23 for multiple curved cracks; (II) (b)-(d) in Figure 4.24 for multiple voids; (III) (b)-(d) in Figure 4.25 for multiple inclusions. Here, $\Lambda_i = \mathcal{L}_i/\mathcal{L}_0$.

C_{III} are appropriately chosen in consideration of computational cost:

$$C_{I(n)}\left(=C_{II(n)}\right)=\frac{\left|\mathcal{L}_{(n-1)}-\mathcal{L}_{(n)}\right|}{\mathcal{L}_{(n)}}\ \leq\ 5\times10^{-4},$$
$$C_{III(n)}:\mathcal{L}_{(n)}\ \leq\ 1.3\times10^{-6}\quad\text{or}\quad\mathcal{P}_{(n)}>17, \tag{4.7}$$

with

$$\mathcal{P}_{(n)}=\begin{cases}2\mathcal{P}_{(n-1)}-1 & \text{with } \mathcal{P}_0=2 & \text{for a curved crack,}\\ 2\mathcal{P}_{(n-1)} & \text{with } \mathcal{P}_0=1,\ \mathcal{P}_1=4 & \text{for a void/inclusion.}\end{cases} \tag{4.8}$$

where $\mathcal{P}_{(n)}$ denotes the total number of shape control points at the n-th step ($n\rightarrow n+1$ in the process of adding shape control points to the current selected scatterer's set in the flowchart). The new control points are positioned along the cubic spline curves connecting the existing control points.

In order to localize multiple unknown scatterers, the divide-and-conquer strategy is used as the first phase. This procedure is identical to that used for detecting a single scatterer. As shown in Figure 4.19, multiple initial estimates 1–18 (orange/blue-colored circles) are uniformly distributed in the computational domain, and the minimization process for each estimate is performed independently until the convergence criterion I (C_I, see Eq. 4.7) is satisfied.

From each of the independent inversions, the converged locations of the initial estimates are displayed with arrows ($\rightarrow$) in the figure wherein the blue dashed-dotted estimates (3, 6, 10, 13 and 16) converge to the same position near each target scatterer (global minimum) while the others (orange-colored estimates 1–18 except 3, 6, 10, 13 and 16) are positioned on various different locations (local minima).

Values of the objective functional at each of the converged estimates are also compared. The histogram in Figure 4.20 shows the quantitative difference of the normalized objective functional values, Λ $\left(\Lambda_i=\frac{\langle\mathcal{L}\rangle-\mathcal{L}_i}{\langle\mathcal{L}\rangle},\ i=1-18,\ \ \langle\rangle \text{ denotes an average quantity}\right)$, between the cases

(colored with blue) that converged to the global minimum and the cases (colored with orange) that fell into local minima. The initial estimates that converged near the target scatterers (the black dashed lines) have relatively low values of $\mathcal{L}$ compared to those that converged to (or wandered into) locations far from the target scatterers. Therefore, we can easily identify and select the candidate sets that converged towards the global minimizers from the set of initial estimates.

In the subsequent (second) phase (i.e., the right-column of the flowchart on Figure **??**), we optimize the shape of each candidate scatterer using cubic splines. As mentioned earlier, the beginning total number of shape control points in this phase for the case of voids/inclusions is changed from $\mathcal{P}_0 = 1$ (i.e., the center point of the circle) to $\mathcal{P}_1 = 4$ (i.e., 4 points on the edge of the circle in the x and y coordinates) by passing through the procedure that adds shape control points to the current chosen scatterer set.

Figure 4.21 illustrates the alternate-and-conquer procedure from (a) to (c): (a) shape optimization is carried out for the scatterer $\boxed{\text{A}}$. Meanwhile, the shape and position of scatterer $\boxed{\text{B}}$ is held fixed; (b) the shape of the scatterer $\boxed{\text{B}}$ with 4 control points is optimized, while the geometry of the scatterer $\boxed{\text{A}}$ is held fixed at its last converged state; (c) the optimization stage (a) is repeated, but this time by using 8 control points. That is, the optimization process alternates between $\boxed{\text{A}}$ and $\boxed{\text{B}}$ (or among multiple candidate scatterers). The variation of the value of $\Lambda_i (= \mathcal{L}_i/\mathcal{L}_0)$ corresponding to iteration number, i, at each stage of the optimization—i.e., (a), (b), and (c)—is shown in Figure 4.22. These results indicate that multiple voids are successfully identified, even though small peaks occur during transitions (e.g., between (a) and (b), and (b) and (c)) due to the small change in the geometry when additional shape control points are inserted. Note that each of the aforementioned iterations entail a series of forward analyses because of the finite difference approximation of the search gradient, and the

backtracking line-search scheme[1].

To investigate the performance and effectiveness of the proposed identification approach for various types of multiple arbitrarily shaped scatterers (cracks, voids, or inclusions) within a homogeneous/heterogeneous medium, numerical studies are performed as shown in Figures 4.23, 4.24, and 4.25. These figures visualize the sequence of convergence for the estimated scatterers: figures (a) display the localization of the estimated scatterers yielded by the divide-and-conquer algorithm (phase 1), and the other figures (b) to (d)/(e) show the iteratively refined shapes of the unknown scatterers obtained through the alternate-and-conquer algorithm (phase 2).

As explained in previous section for the divide-and-conquer approach, the starting geometries of initial estimates (e.g., a straight line for a crack and a circle for a void/inclusion) are determined based on the anticipated types of target scatterers, which can be determined via conventional bulk ultrasonic testing. Then, the candidate estimates in the vicinity of global minimizers are selected and their locations and sizes are approximated in the second phase (see, Figures 4.23.a, 4.24.a, and 4.25.a).

Using the alternate-and-conquer approach subsequently, the geometries of target scatterers are gradually and successfully reconstructed by increasing the number of cubic spline curves as observed in (b) to (d)/(e) of Figure 4.23, 4.24, and 4.25. That is, 3, 5, 9, and 17 number of shape control points are used to respectively represent the curved cracks in Figure 4.23.b-e, while arbitrarily shaped voids/inclusions are described with 4, 8 and 16 number of shape control points in Figure 4.24.b-d, and 4.25.b-d, respectively. Also, the variations of the normalized objective functional ($\Lambda_i = \mathcal{L}_i/\mathcal{L}_0$) are investigated as illustrated in Figure 4.26.I-

[1]Specifically, each iteration denotes forward analyses twice the current total number of shape parameters and the additional (ς) parameters due to the finite difference approximation and the backtracking line-search scheme, respectively. For example, in the case of a circular void/inclusion with 4 control points (i.e., 8 shape parameters), $2 \times 8 + \varsigma$ forward analyses are carried out during each iteration.

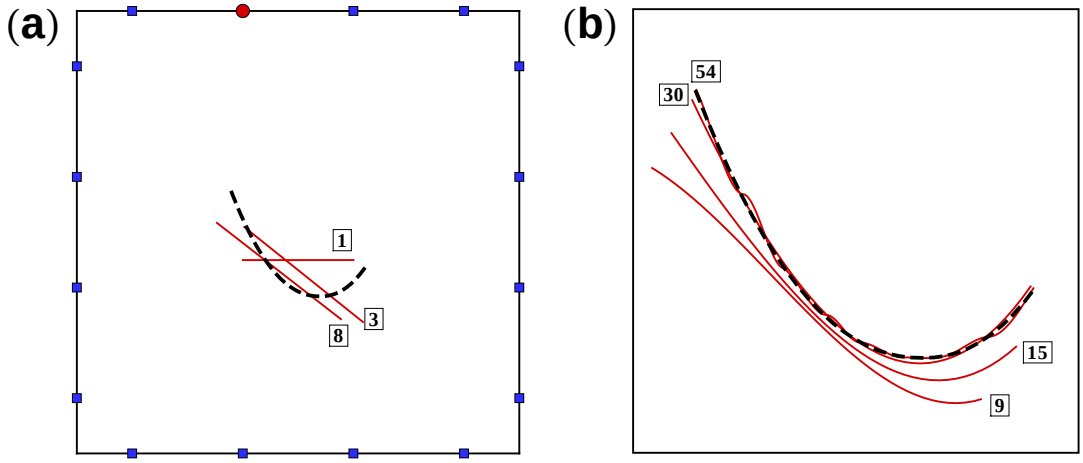

Figure 4.27: Evolutionary detection process for a curved crack (dashed line) using first (a) a straight line, and subsequently (b) cubic splines. The iteration number is shown with a boxed numeral (initially estimated scatterer is marked as 1). Note that the measurements (u^M) were polluted by noise with an amplitude equal to 10% of the root-mean-square of the clean signal).

III corresponding to (b) to (d)/(e) of Figure 4.23, 4.24, and 4.25. It is noted that low or high peaks of Λ appear at the occasions when the new shape control points are inserted to the existing set. This is because the existing geometry of the scatterer is slightly altered in this insertion. However, the said peaks are dramatically and quickly decreased within a few iterations following the insertions.

4.5 Analysis of effect of noise on the identification

In the numerical experiments thus far, the effects of measurement noise or modeling errors on reconstructions were not considered. Herein, an example on the effects of noise on the identification is investigated. For this purpose, we consider the same L-shaped crack used earlier (Fig. 4.12.a) for a single scatterer, but we inject a zero-mean Gaussian random noise with standard deviation that is equal to 10% of the root mean square (RMS) of the original signal into each sensor's

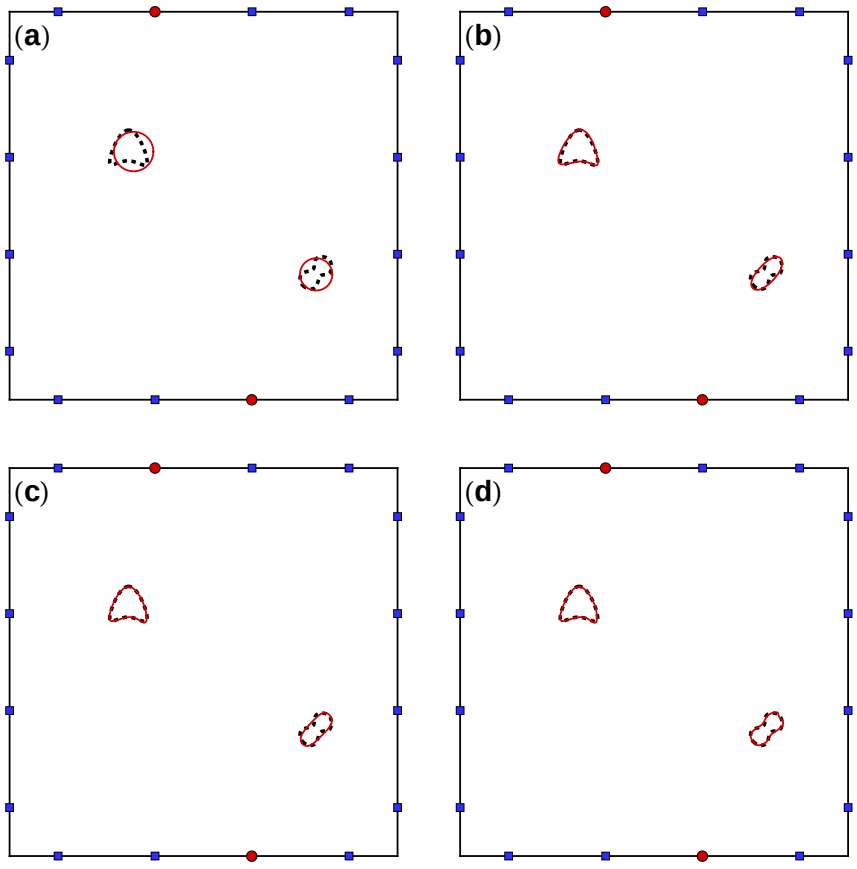

Figure 4.28: Evolutionary identification process for multiple voids (dashed lines) from (a) to (d): (a) the initial-estimated scatterers (solid lines) are localized by using the divide-and-conquer strategy; (b)-(d) the scatterers's shapes are refined by using cubic splines under the alternate-and-conquer strategy. Note that a random noise with 10% of the root-mean-square value of the noise-free signal response is injected into the measurements (u^M).

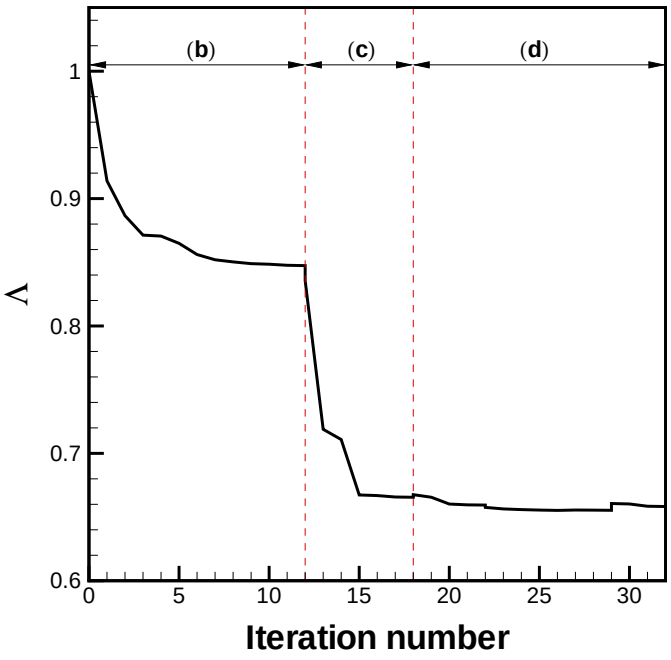

Figure 4.29: The variation of Λ with the iteration number, i, during the detection process (b) to (d) in Figure 4.28 for multiple voids. Here, $\Lambda_i = \mathcal{L}_i/\mathcal{L}_0$.

reading. The results of this numerical experiment are displayed in Figure 4.27. As in the case of the noise-free problem, the identification procedure starts at the initially estimated scatterers' positions marked with 1 and subsequently, converges to the geometry marked with 54. This final converged geometry has five control points. While the number of iterations more than doubled compared to the noise-free case (which required 21 iterations to satisfy the same convergence criteria), the final result is still very accurate under this relatively high noise level.

For multiple scatterers whose sizes are smaller than the scatterers used before—for example, in Figure 4.28—multiple voids with arbitrary shapes are localized (a) and reconstructed (b)-(d) by following the optimization procedure of the divide-alternate-and conquer approach under the same conditions. Figure 4.29 displays the convergence behavior of Λ ($\Lambda_i = \mathcal{L}_i/\mathcal{L}_0$) in each subprocess ((b)-(d)) of the alternate-and-conquer approach. The value of Λ during the period between (b) and (c) sharply declines, while its value in the period (d) is almost retained due to the effect of the injected noise. In spite of the relatively high level of the noise, the finally converged geometries are still fairly accurate as visualized in Figure 4.28.d.

CHAPTER 5

Concluding Remarks

A systematic numerical approach is presented for localization and shape identification of the multiple internal scatterers (such as cracks, voids, or inclusions) with arbitrary shapes in a homogeneous/heterogeneous elastic host medium.

For the forward problems, a dynamic XFEM approach endowed with parametric representation (here cubic splines) of internal boundaries is devised. This combination allows updating the unknown geometry of a scatterer without remeshing during an iterative identification procedure.

For the inverse problems, the unknown shape parameters of each scatterer are optimized based on a gradient-based minimization method that is enhanced with a divide-alternate-and-conquer approach. This combination enables localization and shape identification of multiple scatterers, while avoiding local minima.

Numerical experiments involving various types of multiple arbitrarily shaped scatterers clearly demonstrate the effectiveness and accuracy of proposed numerical techniques. The overall approach is also shown to be robust against fairly large values of measurement noise.

Possible future extensions of this work include:

- *Experimental validation*: The proposed methods should be validated using real-life experimental data. The experiments can mimic the numerical examples provided in this thesis.

- *Three-dimensional problems*: This avenue may be pursued by employing the

so-called NURBS to represent the geometry of three-dimensional inclusions (Cottrell et al., 2009; Sevilla et al., 2011).

- *Medical imaging and identification*: The burgeoning field of "elasticity imaging" appears to yield data that can be used to localize and identify tumors (Urban et al., 2011) with the proposed methods.

- *Property identification*: The elastic/viscoelastic material properties of the inclusions could be determined along with their shapes and locations.

- *Optimizing the computational performance*: The methods proposed here can be optimized to enhance numerical performance, especially by exploiting the apparent granularity of the divide-and-conquer algorithm through parallel programming.

- *Absorbing boundary conditions*: In most real life problems, signals attenuate due to material and geometric damping. It would be expedient to implement absorbing boundary representations, such as Perfectly Matched Layers (Kucukcoban and Kallivokas, 2011), to handle such problems.

APPENDIX A

Auxiliary Stress Fields

The auxiliary stresses derived by Westergaard (1939) and Williams (1957) are

$$\sigma_{11} = \frac{1}{\sqrt{2\pi r}} \left\{ K_I \; cos\frac{\theta}{2} \left[1 - sin\frac{\theta}{2} sin\frac{3\theta}{2} \right] - K_{II} \; sin\frac{\theta}{2} \left[2 + cos\frac{\theta}{2} cos\frac{3\theta}{2} \right] \right\} \tag{A.1}$$

$$\sigma_{22} = \frac{1}{\sqrt{2\pi r}} \left\{ K_I \; cos\frac{\theta}{2} \left[1 + sin\frac{\theta}{2} sin\frac{3\theta}{2} \right] + K_{II} \; sin\frac{\theta}{2} cos\frac{\theta}{2} cos\frac{3\theta}{2} \right\} \tag{A.2}$$

$$\sigma_{33} = \nu(\sigma_{11} + \sigma_{22}) \tag{A.3}$$

$$\sigma_{23} = \frac{1}{\sqrt{2\pi r}} K_{III} cos\frac{\theta}{2} \tag{A.4}$$

$$\sigma_{31} = \frac{-1}{\sqrt{2\pi r}} sin\frac{\theta}{2} \tag{A.5}$$

$$\sigma_{12} = \frac{1}{\sqrt{2\pi r}} \left\{ K_I \; sin\frac{\theta}{2} cos\frac{\theta}{2} cos\frac{3\theta}{2} + K_{II} \; cos\frac{\theta}{2} \left[1 - sin\frac{\theta}{2} sin\frac{3\theta}{2} \right] \right\} \tag{A.6}$$

and the auxiliary displacements are

$$u_1 = \frac{1}{2\mu} \sqrt{\frac{r}{2\pi}} \left\{ K_I \; cos\frac{\theta}{2} (k - cos\theta) + K_{II} \; sin\frac{\theta}{2} (k + 2 + cos\theta) \right\} \tag{A.7}$$

$$u_2 = \frac{1}{2\mu} \sqrt{\frac{r}{2\pi}} \left\{ K_I \; sin\frac{\theta}{2} (k - cos\theta) - K_{II} \; cos\frac{\theta}{2} (k + 2 + cos\theta) \right\} \tag{A.8}$$

$$u_2 = \frac{1}{2\mu} \sqrt{\frac{r}{2\pi}} K_{III} \; sin\frac{\theta}{2} \tag{A.9}$$

where μ is the shear modulus and k is the Kosolov constant.

APPENDIX B

The J- and Interaction Integrals

The domain forms of the interaction integrals are used to calculate the mixed-mode stress intensity factors. J-integral is a method of calculating the strain energy release rate, and the independent property on its path helps to evaluate the integral in the far-field with the crack-tip. For a general mixed-mode situation, the J-integral is related to the stress intensity factors ($K_I,\ K_{II}$) as

$$J = \frac{K_I^2}{E^*} + \frac{K_{II}^2}{E^*} \tag{B.1}$$

where

$$E^* = \begin{cases} E & \text{for plane stress} \\ \frac{E}{1-\nu^2} & \text{for plane strain} \end{cases} \tag{B.2}$$

where E is Young's modulus and ν is Poisson's ratio. The J-integral takes the form

$$J = \int_\Gamma \left(W n_i - \sigma_{jk} n_j \frac{\partial u_k}{\partial x_i} \right) d\Gamma \tag{B.3}$$

where W is the strain energy density. Eq. (B.3) can be written in the equivalent form using the Dirac delta, which is easier to implement in finite element code as

$$J = \int_\Gamma \left(W \delta_{1i} - \sigma_{ij} \frac{\partial u_i}{\partial x_1} \right) n_j d\Gamma \tag{B.4}$$

In order to calculate the mixed-mode stress intensity factors, an auxiliary stress state is superimposed onto the stress and displacement fields from the XFEM analysis. The auxiliary stress and displacement states at the crack-tip are introduced by Westergaard (1939) and Williams (1957) for a homogeneous crack, and

by Sukumar *et al.* (2001) for the case of a bi-material crack, which are given in Appendix A.

Hereafter, the XFEM states are denoted with superscript (1) as $u_{ij}^{(1)}$, $\varepsilon_{ij}^{(1)}$ and $\sigma_{ij}^{(1)}$, while that from the auxiliary state as $u_{ij}^{(2)}$, $\varepsilon_{ij}^{(2)}$ and $\sigma_{ij}^{(2)}$. The J-integral for the two superposed states is

$$J^{(1+2)} = \int_{\Gamma} \left(\frac{1}{2}(\sigma_{ij}^{(1)} + \sigma_{ij}^{(2)})(\varepsilon_{ij}^{(1)} + \varepsilon_{ij}^{(2)})\delta_{1i} - (\sigma_{ij}^{(1)} + \sigma_{ij}^{(2)}) \frac{\partial (u_i^{(1)} + u_i^{(2)})}{\partial x_1} \right) n_j d\Gamma \tag{B.5}$$

The J-integrals for the pure state 1 and the auxiliary state 2 can be separated in Eq. (B.5), which leaves an interaction term such that

$$J_i^{(1+2)} = J_1^{(1)} + J_1^{(2)} + I^{(1,2)} \tag{B.6}$$

where $I^{(1,2)}$ is the interaction integral and is given by

$$I^{(1,2)} = \int_{\Gamma} \left[W^{(1,2)}\delta_{1j} - \sigma_{ij}^{(1)} \frac{\partial u_i^{(2)}}{\partial x_1} - \sigma_{ij}^{(2)} \frac{\partial u_i^{(1)}}{\partial x_1} \right] n_j d\Gamma \tag{B.7}$$

where $W^{(1,2)}$ is the interaction strain energy density

$$W^{(1,2)} = \sigma_{ij}^{(1)} \varepsilon_{ij}^{2)} = \sigma_{ij}^{(2)} \varepsilon_{ij}^{(1)} \tag{B.8}$$

Recalling the relationship between J and K, we can write Eq. (B.1) as

$$J_1^{(1+2)} = \frac{(K_I^{(1)} + K_I^{(2)})^2}{E^*} + \frac{(K_{II}^{(1)} + K_{II}^{(2)})^2}{E^*} \tag{B.9}$$

Expanding and rearranging terms from the above equation yields

$$J_1^{(1+2)} = J_1^{(1)} + J_1^{(2)} + \underbrace{\frac{2(K_I^{(1)} + K_I^{(2)} + K_{II}^{(1)} + K_{II}^{(2)})}{E^*}}_{I^{(1,2)}} \tag{B.10}$$

The stress intensity factors for the current state can be obtained by separating the two modes of fracture. By setting $K_I^{(2)} = 1$ and $K_{II}^{(2)} = 0$, so that $K_I^{(1)}$ is given by

$$K_I^{(1)} = \frac{I^{(1,ModeI)} E^*}{2} \tag{B.11}$$

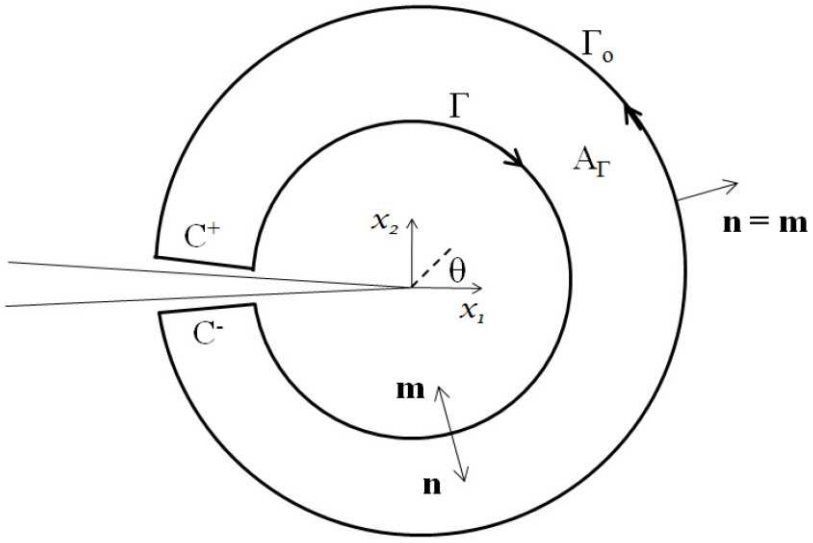

Figure B.1: Conventions for domain J: domain A is enclosed by Γ, $C^{\pm}$ and Γ_0. Unit normal $m_j = n_j$ on Γ_0 and $m = -n_j$ on Γ.

A similar procedure, $K_I^{(2)} = 0$ and $K_{II}^{(2)} = 1$, can also be followed such that $K_I^{(1)}$ is

$$K_{II}^{(1)} = \frac{I^{(1,ModeII)} E^*}{2} \tag{B.12}$$

The contour integral mentioned above is not in a form best suited to finite element calculations. A weighting function Q is introduced so that it has a value equal to unity on the contour Γ and zero at the outer contour Γ_0 as shown in Fig. B.1.

Within the area enclosed by a closed path Γ, Γ_0, and $C^{\pm}$, the weighting function Q is an arbitrary smooth function varying in between zero and unity. The interaction integral for a closed path $C = \Gamma \cup C^+ \cup \Gamma_0 \cup C^-$ can be written as

$$I^{(1,2)} = \int_C \left[W^{(1,2)} \delta_{1j} - \sigma_{ij}^{(1)} \frac{\partial u_i^{(2)}}{\partial x_1} - \sigma_{ij}^{(2)} \frac{\partial u_i^{(1)}}{\partial x_1} \right] Q m_j d\Gamma \tag{B.13}$$

where m_j are components of unit normal vector to the closed curve C acting

outward to the area A. It should be noted here that $m_j = -n_j$ on the contour Γ and $m_j = n_j$ on Γ_0, and $C^{\pm}$. The crack faces are considered to be traction free. Using the divergence theorem and passing the limit to the crack-tip, we get

$$I^{(1,2)} = \int_A \left[-W^{(1,2)}\delta_{1j} + \sigma_{ij}^{(1)} \frac{\partial u_i^{(2)}}{\partial x_1} + \sigma_{ij}^{(2)} \frac{\partial u_i^{(1)}}{\partial x_1} \right] \frac{\partial Q}{\partial x_j} dA \tag{B.14}$$

Bibliography

A. Bagheri, G. G. Amiri, and S. A. S. Razzaghi. Vibration-based damage identification of plate structures via curvelet transform. *J. Sound and Vibration*, 327: 593–603, 2009.

W. Bayissa and N. Haritos. Structural damage identification in plates using spectral strain energy analysis. *J. Sound and Vibration*, 307:226–249, 2007.

W. Bayissa, N. Haritos, and W. Thelandersson. Vibration-based struc- tural damage identification using wavelet transform. *Mechanical Systems and Signal Processing*, 22:1194–1215, 2008.

T. Belytschko and T. Black. Elastic crack growth in finite elements with minimal remeshing. *Int. J. Numer. Methods Eng.*, 45:601–620, 1999.

T. Belytschko and R. Gracie. On xfem applications to dislocations and interfaces. *Int. J. Plast.*, 23:1721–1738, 2007.

T. Belytschko, N. Moës, S. Usui, and C. Parimi. Arbitrary discontinuities in finite elements. *Int. J. Numer. Methods Engrg.*, 50:993–1013, 2001.

T. Belytschko, R. Gracie, and G. Ventura. A review of extended/generalized finite element methods for material modeling. *Model. Simul. Mater. Sci. Engrg.*, 17 (043001), 2009.

B. A. Benowitz and H. Waisman. A spline-based enrichment function for arbitrary inclusions in extended finite element method with applications to finite deformations. *Int. J. Numer. Methods Eng.*, 95:361–386, 2013.

M. Bonnet and B. Guzina. Elastic-wave identification of penetrable obstacles using shape-material sensitivity framework. *J. Comput. Phys.*, 228:294–311, 2009.

J. C. Brigham, W. Aquino, F. G. Mitri, J. F. Greenleaf, and M. Fatemi. Inverse estimation of viscoelastic material properties for solids immersed in fluids using vibroacoustic techniques. *J. Appl. Phys.*, 101(023509), 2007.

E. N. Chatzi, B. Hiriyur, H. Waisman, and A. W. Smyth. Experimental application and enhancement of the xfem-ga algorithm for the detection of flaws in structures. *Comput. Struct.*, 89:556–570, 2011.

J. Cottrell, T.J.R. Hughes, and Y. Basilevs. *Isogeometric analysis: Toward Unification of CAD and FEA*. John Wiley and Sons, 2009.

S. W. Doebling, Farrar C. R., and M. B. Prime. A summary review of vibration-based damage identification methods. *Shock Vib. Dig.*, 30(2):91–105, 1998.

J. Dundurs. Edge-bonded dissimilar orthogonal elastic wedges. *J. Appl. Mech.*, 36:650–652, 1969.

H. Edelsbrunner. *Geometry and Topology for Mesh Generation*. Cambridge University Press, 2001.

Y. Fan, T. Jiang, and D. J. Evans. The parallel genetic algorithm for electromagnetic inverse scattering of a conductor. *Int. J. Computer Math.*, 79:573–586, 2002.

M. Fatemi and J. F. Greenleaf. Vibro-acoustography: An imaging modality based on ultrasound-stimulated acoustic emission. *Proc. Natl. Acad. Sci. USA*, 96: 6603–6608, 1999.

E. M. Feericka, X. C. Liub, and P. McGarrya. Anisotropic mode-dependent damage of cortical bone using the extended finite element method (xfem). *J. Mech. Behav. Biomed. Mater.*, 20:77–89, 2013.

M. Fleming, Y. A. Chu, B. Moran, and T. Belytschko. Enriched element-free galerkin methods for crack tip fields. *Int. J. Numer. Methods Eng.*, 40:1483–1504, 1997.

L. B. Freund. *Dynamic Fracture Mechanics*. Cambridge University Press, Cambridge: UK, 1990.

T. P. Fries and T. Belytschko. The extended/generalized finite element method: an overview of the method and its applications. *Int. J. Nu- mer. Methods Eng.*, 84:253–304, 2010.

D. Goldberg. *Genetic Algorithms in Search, Optimization and Machine Learning*. Addison-Wesley, Reading, MA, 1989.

K. F. Graff. *A History of Ultrasonics, in Physical Acoustics*, volume XV. Academic Press, New York, 1982.

C. J. Hellier. *Handbook of Nondestructive Evaluation*. McGraw-Hill, NY, 2003.

Y. Hirano and K. Okazaki. Vibration of cracked rectangular plates. *Bull. JSME*, 23(179):732–740, 1980.

K. D. Hjelmstad. On the uniqueness of modal parameter estimation. *J. Sound Vib.*, 192(2):581–598, 1996.

H. Jia, T. Takenaka, and T. Tanaka. Time-domain inverse scattering method for cross-borehole radar imaging. *IEEE Trans. on Geoscience and Remote Sensing*, 40:1640–1647, 2002.

V. Juneja, R. T. Haftka, and H. H. Cudney. Damage detection and damage detectability: Analysis and experiments. *J. Aerospace Engng.*, 104:135–142, 1997.

J. Jung. Development of an extended-semi-analytical finite element (xsafe) method for damage quantification in heterogeneous anisotropic waveguides. A prospectus for the degree of doctor of philisophy in mechanical and aerospace engineering, University of California, Los Angeles, 2011.

J. Jung and E. Taciroglu. Modeling and identification of an arbitrarily shaped scatterer using dynamic xfem with cubic splines. *Comput. Methods Appl. Mech. Eng.*, 278:101–118, 2014.

J. Jung, C. Jeong, and E. Taciroglu. Identification of a scatterer embedded in elastic heterogeneous media using dynamic xfem. *Comput. Methods Appl. Mech. Eng.*, 259:50–63, 2013.

L. F. Kallivokas, A. Fathi, S. Kucukcoban, K. H. Stokoe II, J. Bielak, and O. Ghattas Ghattas. Site characterization using full waveform inversion. *Soil Dyn. Earthq. Eng.*, 47:62–82, 2013.

D. Karaboga. An idea based on honey bee swarm for numerical optimization. Technical Report Technical Report-TR06, Erciyes University, Computer Engineering Department, Kayseri, Turkey, 2005.

J. Krautkrämer and H. Krautkrämer. *Ultrasonic testing of materials*. Springer-Verlag, Berlin, New York, 1990.

S. Kucukcoban and L. F. Kallivokas. Mixed perfectly-matched-layers for direct transient analysis in 2d elastic heterogeneous media. *Computer Methods in Applied Mechanics and Engineering*, 200(1):57–76, 2011.

J. M. Lifshitz and A. Rotem. Determination of reinforcement un- bonding of composites by a vibration technique. *J. Compos. Mater.*, 3:412–423, 1969.

G. R. Liu and X. Han. *Computational Inverse Techniques in Nondestructive Evaluation*. CRC Press, Boca Raton, FL, 2003.

P. P. Lynn and N. KumbasaR. Free vibration of thin rectangular plates having narrow cracks with simply supported edges. *Dev. Mech.*, 4:911–928, 1967.

J. M. Melenk and I. Babuška. The partition of unity finite element method: Base theory and the partition of unity finite element method: Base theory and the partition of unity finite element method: Base theory and applications. *Comput. Methods Appl. Mech. Engrg.*, 39:289–314, 1996.

T. Menouillard, J. Song, Q. Duan, and T. Belytschko. Time dependent crack tip enrichment for dynamic crack propagation. *Int. J. Fracture*, 162:33–49, 2010.

N. Moës, M. Cloirec, P. Cartraud, and J. F. Remacle. A computational approach to handle complex microstructure geometries. *Comput. Methods Appl. Mech. Eng.*, 192:3163–3177, 2003.

J. Nocedal and S. J. Wright. *Numerical Optimization*. Springer-Verlag, New York, 2nd edition, 2006.

D. Rabinovich, D. Givoli, and S. Vigdergauz. Xfem-based crack detection scheme using a genetic algorithm. *Int. J. Numer. Methods Eng.*, 71:1051–1080, 2007.

D. Rabinovich, D. Givoli, and S. Vigdergauz. Crack identification by arrival time using xfem and a genetic algorithm. *Int. J. Numer. Methods Eng.*, 77:337–359, 2009.

J. R. Rice and G. C. Sih. Plane problems of cracks in dissimilar media. *J. Appl. Mech.*, 32:418–423, 1965.

C. L. Richardson, J. Hegemann, E. Sifakis, J. Hellrung, and J. M. Teran. An xfem method for modeling geometrically elaborate crack propagation in brittle materials. *Int. J. Numer. Methods Eng.*, 88:1042–1065, 2011.

P. Rizzo and F. Lanza di Scalea. Ultrasonic inspection of multi-wire steel strands with the aid of the wavelet transform. *Smart Materials and Structures*, 14: 685–695, 2005.

J. H. Rose. Elastic wave inverse scattering in nondestructive evaluation. *Pure Appl. Geophys.*, 131:715–739, 1989.

M. Rucka and K. Wilde. Application of continuous wavelet transform in vibration based damagedetection method for beams and plates. *J. Sound and Vibration*, 297:536–550, 2006.

H. Sauerland and T. P. Fries. A stable xfem for two-phase flows. *Comput. Fluids*, 87:41–49, 2013.

R. Sevilla, S. Fernandez-Mendez, and A. Huerta. Nurbs-enhanced finite element method (nefem). *Archives of Computational Methods in Engineering*, 18(4): 441–484, 2011.

P. J. Shull. *Nondestructive Evaluation: Theory, Techniques, and Applications*. Marcel Dekker Inc., 2002.

B. G. Smith, B. L. Vaughan, and D. L. Chopp. The extended finite element method for boundary layer problems in biofilm growth. *Comm. App. Math. and Comp. Sci.*, 2(1), 2007.

S. Y. Sokolov. Ultrasonic methods of detecting internal flaws in metal articles. *Zavodskaya Laboratoriya*, 4(1468-1472), 1935.

N. Sukumar, D. L. Chopp, N. Moës, and T. Belytschko. Modeling holes and inclusions by level sets in the extended finite-element method. *Comput. Methods Appl. Mech. Eng.*, 190:6183–6200, 2001.

N. Sukumar, Z. Y. Huang, J. H. Prévost, and Z. Suo. Partition of unity enrichment for partition of unity enrichment for bimaterial interface cracks. *Int. J. Numer. Methods Eng.*, 59:1075–1102, 2004.

H. Sun, H. Waisman, and R. Betti. Nondestructive identification of multiple flaws using xfem and a topologically adapting artificial bee colony algorithm. *Int. J. Numer. Methods Eng.*, 95:871–900, 2013.

M. W. Urban, A. Alizad, W. Aquino, J. F. Greenleaf, and M. Fatemi. A review of vibro-acoustography and its applications in medicine. *Cur. Medical Imaging Rev.*, 7:350–359, 2011.

H. Waisman, E. Chatzi, and A. W. Smyth. Detection and quantification of flaws in structures by the extended finite element method and genetic algorithms. *Int. J. Numer. Methods Eng.*, 82:303–328, 2010.

H.M. Westergaard. Bearing pressures and cracks. *Journal of Applied Mechanics*, 6:49–53, 1939.

K. V. Wijk. *Multiple scattering of surface waves*. PhD thesis, Department of geophysics, Colorado school of mines at Golden, Colorado, 80401, 2003.

M.L. Williams. On the stress distribution at the base of a stationary crack. *Journal of Applied Mechanics*, 24(109-114), 1957.

E. Yu, J. W. Wallace, and E. Taciroglu. Parameter identification of framed structures using an improved finite element model-updating method—part ii: Application to experimental data. *Earthquake Engineering and Structural Dynamics*, 36:641–660, 2007.

H. Yuan and B. B. Guzina. Topological sensitivity for vibro-acoustography applications. *Wave Motion*, 49:765–781, 2012.

Y. Zou, L. Tong, and G. P. Steven. Vibration-based model-dependent damage (delamination) identification and health monitoring for composite structures-a review. *J. Sound Vib.*, 230:357–378, 2000.